

Shocks and Corresponding Physical
Properties of Merging Galaxy Clusters in
Magneticum



Bachelor thesis at the Faculty of Physics
Ludwig-Maximilians-University Munich

Submitted by

Julian Silvester Sommer

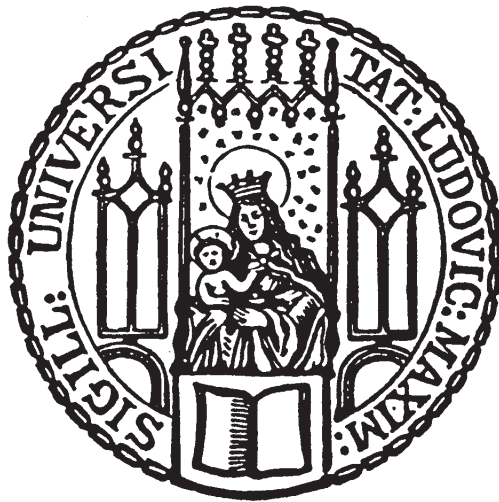
Supervised by

PD Dr. habil. Klaus Dolag

Ludwig Maximilian Böss

Munich, 16th of July 2021

Schockwellen und ihre physikalischen
Eigenschaften von kollidierenden
Galaxienhaufen in *Magneticum*



Bachelorarbeit der Fakultät für Physik der
Ludwig-Maximilians-Universität München

Vorgelegt von

Julian Silvester Sommer

Betreut von

PD Dr. habil. Klaus Dolag

Ludwig Maximilian Böss

München, den 16.07.2021

Contents

1	Introduction	1
1.1	Motivation	1
1.2	Physical Properties of Shocks and their Detection	2
1.2.1	The Sunyaev-Zeldovich Effect	2
1.2.2	Scaling of X-ray Emissions	4
1.2.3	Rankine-Hugoniot Jump Conditions	5
1.2.4	Morphology of Shocks in Merging Galaxy Clusters	6
1.2.5	Radio Relics as an Indication of Shocked Gas in the ICM	7
1.3	Redshift as a Representation of Time	7
2	Methodology	9
2.1	Magneticum and its Applications	9
2.1.1	Cluster Find	9
2.1.2	SMAC	10
2.2	Extracting Physical Values from FITS Files	10
2.2.1	Calculating Distances	11
2.2.2	Measuring Distances and Physical Values with <i>SAO Image DS9</i>	12
2.3	Radial Binning	13
2.4	Gaussian Filtering	13
3	The Offset of SZ and X-ray Positions in Merging Clusters	15
3.1	Constellations of Shock Morphologies	15
3.2	Comparison of SZ-X-ray Peak Offsets of Simulated Clusters to the Observed Cluster PLCK G200.9-28.2	16
3.3	Investigation of SZ and X-ray Centroids	19
4	The Offset of Total Mass Density Positions in Merging Cluster	23
4.1	Morphological Evolution of Mass Distributions over Time	23
4.2	Distribution of Total Mass Density Offset Centroids	23
4.3	Correlation of SZ, X-ray and TMD Offsets	25

5 Discussion	29
5.1 Conclusion	29
5.1.1 Assignment of Selective Surface Brightness Peaks and Centroid Offsets	29
5.1.2 Observational Feasibility	30
5.2 Outlook	30
Appendices	41
A Data Tables	43
A.1 List of Merging Clusters with Detected Shocks	43
B Derivations	47
B.1 Photon's Energy After Inverse Compton Scattering	47
B.2 Rankine-Hugoniot Jump Conditions	49

Chapter 1

Introduction

1.1 Motivation

High pressure differences are expected to appear in the peripheries of merging galaxy clusters, which occur due to the compressions of the intracluster medium (ICM) by infalling galaxy sub-clusters towards their potential minimum. By considering a perfect head-on collision, one can imagine a scenario of a bullet flying through a target and compressing the surrounding medium due to the projectile's high velocity relative to the target. In an astrophysical setting, the bullet can be associated with a highly energetic, small galaxy subcluster. The target is represented by a more massive subcluster, which gravitationally pulls the surrounding material, i.e., other subclusters towards its potential minimum. Once the infallen substructures collide with the target's core, the compressed ICM forms shock waves, which propagate towards the peripheries of the galaxy cluster and finally dissipate. Those shock waves occur due to high pressure differences over a small distance. Head-on collisions are merger scenarios, where two subclusters collide perfectly on a common axis. Considering this scenario, the morphology can clearly be assigned to an arc-like shape pointing outwards the location where the merger occurred. In Figure 1.1, an ideal head-on collision is illustrated. It should be noted that shocked gas always escapes along the path of least resistance. Hence, equatorial shocks perpendicular to the collision axis arise in low-density regions once the projectile hits the target. After the two components have passed their barycenter, two axial shocks moving towards the outer regions can be expected (Ha et al., 2018).

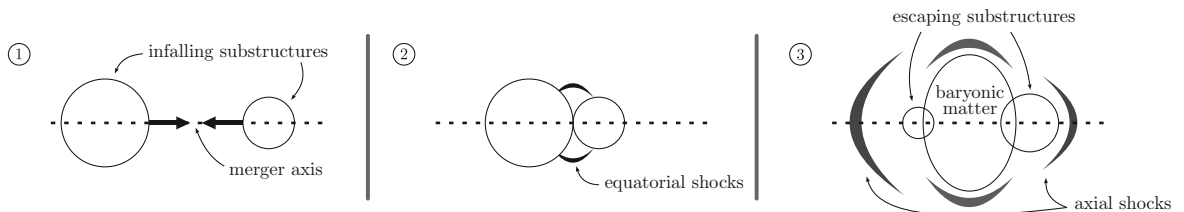


Figure 1.1: An illustration of an ideal head-on collision of two infalling substructures.

In frame (3) the escaping substructure, which consists of dark matter (DM) separate from the baryonic matter (Ha et al., 2018). This leads to an offset of the visible matter relative to the cluster's potential minimum, which, for instance can be verified by observing the X-ray spectra in conjunction with the gravitational lensing effects (Ha et al., 2018). This displacement can be observed in 1E0657-56, also known as the *Bullet Cluster* and was reproduced in high-resolution smoothed-particle hydrodynamics simulations (SPH) by Mastropietro and

Burkert (2008). However, not only an offset in the X-ray spectra, but also in the position of the Sunyaev-Zeldovich effect (SZ effect) (Sunyaev and Zeldovich, 1970) from the X-ray peak towards the direction of a radio relic - based on an observation of the galaxy cluster PLCK G200.9-28.2 - could be asserted (Kale et al., 2017). These observations may indicate an ongoing galaxy cluster merger. By analyzing the offset properties, even the state of the merger could be studied. Using the hydrodynamic simulation *Magneticum*¹ (Dolag et al. 2016, in prep) and the tool SMAC (Dolag et al., 2005) in particular, allows a visible detection of an offset of baryonic matter in comparison to the galaxy cluster's DM core. Here, the integrated SUBFIND algorithm locates the potential minimum of the most massive subcluster, such that the output files of galaxy clusters are centered to the gravitational centroid of the heaviest substructure (Dolag et al., 2009). This enables the measurement of radiation-peak-offsets and their comparison with the shock's morphology (see Figure 1.2). A closer look at the shock's properties is going to be taken in the next section.

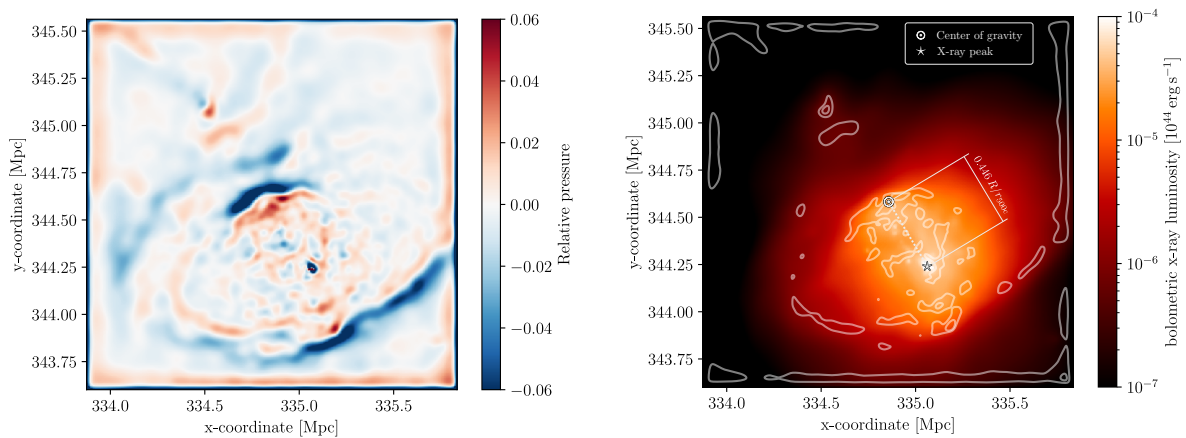


Figure 1.2: Example of a merging galaxy cluster accommodating an offset X-ray peak relative to its potential minimum. This cluster hosts shocks and was extracted from the tool SMAC of the cosmological simulation *Magneticum*.

1.2 Physical Properties of Shocks and their Detection

Shocks indicate an ongoing merger of two galaxy clusters or substructures, since an object collision is directly linked to a compression of the gas in between. Hence, jumps in pressure, temperature and density would be expected. Since shocks are not visible by the naked eye and are characterized by their relative pressure peaks, the question may arise how they can be detected. The close correlation of pressure and the SZ effect is going to be described in the following subsection.

1.2.1 The Sunyaev-Zeldovich Effect

During the early stages of the universe (around $3.8 \cdot 10^5$ years after the big bang (Schneider, 2006, 17)) light was emitted due to the recombination of hydrogen. Since the universe is expanding in an accelerating manner, the initial emission of radiation in the visible spectra was more and more shifted towards lower frequencies, until it reached the microwave spectrum. Today, this isotropic and homogeneous radiation, which is called the cosmic microwave background radiation (CMBR) or cosmic microwave background (CMB), can be detected from

¹<http://www.magneticum.org>

arbitrary directions. Travelling through space, the light can be perturbed in wavelength and direction due to different kinds of obstacles, e.g., the bending of light rays in close proximity of high-mass objects (better known as gravitational lensing effects). In our case, the more interesting perturbation phenomenon is the effect of shifting the CMBR towards higher frequencies as a result of scattering. Once the light rays propagate through the ICM, they can be scattered by high energetic, charged particles like electrons (see Figure 1.3).

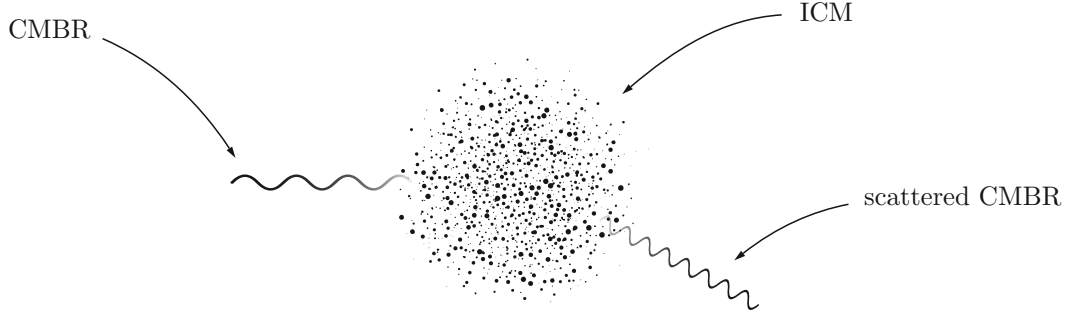


Figure 1.3: Scattered CMBR by electrons in the ICM.

The ICM mainly consists of ionized hydrogen and helium, where the electrons are independently moving apart from their nuclei. Because of the low particle density of approximately 10^{-3} cm^{-3} , the electrons cannot dissipate energy efficiently. Hence, the plasma reaches temperatures of approximately $3 \cdot 10^7 \text{ K}$ (Schneider, 2006, 225). However, there remains a small amount of electrons which dissipate energy by scattering photons, a process which is known as inverse Compton scattering (Carroll, 2014, 1333). In this case, photons coming from the CMB and are consecutively shifted to smaller wavelengths by each scattering process. The energy increase of the photon can be calculated by considering the four-momentums of relativistic photons and electrons. In order to obtain the desired result, the energy-momentum relation and conservation of momentum needs to be calculated. Following the steps in B.1 leads to the energy of the scattered photon, which is partially oriented on (Kolanoski and Wermes, 2016, 80-84):

$$E'_\gamma = \frac{E_\gamma(1 - \beta \cos \psi)}{(1 - \beta \cos \psi') + \frac{E_\gamma}{E_e}(1 - \cos \varphi)} \quad (1.1)$$

In Figure 1.4, the scattering process is illustrated in detail. Here, the angles between the propagation directions of the electron and photon before and after scattering are given by ψ and ψ' , respectively. The angle of the photon before and after scattering is labeled as φ .

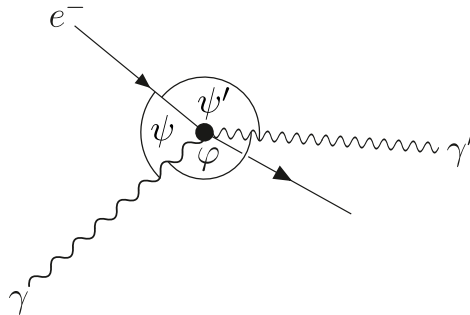


Figure 1.4: A geometric sketch of the inverse Compton scattering.

There are multiple reasons why the SZ effect is a reliable tool for detecting hot cluster gas.

First, the CMB is isotropically distributed, which means that the amount of scattered photons remains statistically conserved. In addition, one could expect that strongly redshifted galaxy clusters would make an SZ signal detection harder, than closer objects. It is important to keep in mind, that the CMB is almost a perfect black body (Konar et al., 2021). An energy spectrum shifted by the SZ effect is detectable independently from its distance, whereas a greater redshift would not effect the strength of the black body spectrum shift towards higher energies (Carlstrom et al., 2002). This, however, does not explain the connection between the pressure and the amount of scattered photons.

In general, the SZ effect tells us something about the intensity shift towards higher frequencies $\Delta I(x)$ compared to its initial intensity $I(x)$, with x being the reduced frequency:

$$x = \frac{h\nu}{k_B T_{\text{rad}}} \quad (1.2)$$

This relation can be expressed as follows (Longair, 2011, 257):

$$\frac{\Delta I(x)}{I(x)} = y \frac{x e^x}{e^x - 1} \left(x \frac{e^x + 1}{e^x - 1} - 4 \right) \quad (1.3)$$

In Magneticum, however, the values of the SZ effect output data are given in units of the Compton- y -parameter, which consists of an integral over the density of electrons n_e , the electron's temperature T_e along the line of sight of the considered galaxy cluster, and various constants.

$$y = \frac{k_B \sigma_T}{m_e c^2} \int n_e T_e dl \quad (1.4)$$

With the Boltzmann constant k_B , the electron's mass m_e , the speed of light c and the Thomson cross-section σ_T . In this case, T_e is the temperature of the ICM.

According to Planelles et al. (2017), the product of n_e and T_e is proportional to the electron's pressure:

$$n_e T_e \propto P_e \quad (1.5)$$

Therefore, the Compton- y -parameter can be interpreted as the pressure integral along the line of sight.

1.2.2 Scaling of X-ray Emissions

In galaxy clusters, Thermal Bremsstrahlung constitutes the main X-ray source. Here, electrons emit radiation, once they get decelerated or even accelerated due to the Coulomb fields of atomic nuclei or protons. Since these ionized particles mostly originate in hot plasmas, it is also expected that Thermal Bremsstrahlung is the main radiation mechanism of X-rays in the hot cluster gas, i.e., the ICM (Schneider, 2006, 244).

Without going into further details, the X-ray luminosity density \mathcal{L}_{vol} , as described by (Carroll, 2014, 1165), is given by:

$$\mathcal{L}_{\text{vol}} = 1.42 \cdot 10^{-28} n_e^2 T^{1/2} \text{Wm}^{-3} \propto n_e^2 \quad (1.6)$$

Here, the electron's density again strongly relates to the density of the ICM. Now, as the scaling relations of the SZ effect and pressure and X-ray and the ICM's density are set up, other important thermodynamic properties, like the shock's mach number M can be derived. Their relation with other thermodynamic states is described by the so-called Rankine-Hugoniot jump conditions.

1.2.3 Rankine-Hugoniot Jump Conditions

The conditions of shocked gas can be described by the ratios of the density ρ , temperature T and pressure p in the up- and downstream. It should be stressed that those differences in the shock's boundaries occur over small distances, which let the jump of two arbitrary conditions appear like a discontinuous change of state (see Figure 1.5).

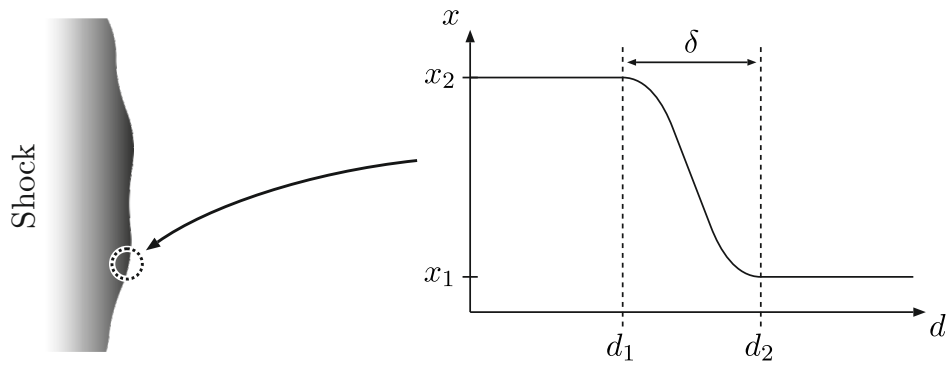


Figure 1.5: Sketch of a shockwave propagating along the distance d . In the limit, the shock originates from a discontinuous jump between the two different states x_1 and x_2 over a small limiting process δ .

These boundaries are determined by the up- and downstream. The shock front is being crossed by particles moving from the upstream towards the downstream and getting scattered back and forth. From the reference frame of the shock wave, the unperturbed particles appear to become turbulent right after they passed the shock front. An illustration of up- and downstream is shown in Figure 1.6.

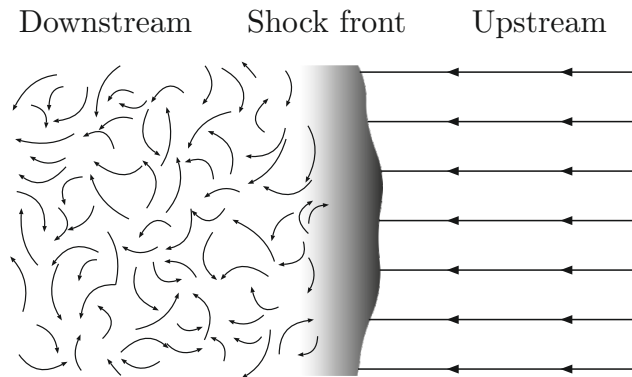


Figure 1.6: Perturbation of particles after crossing the shock region. The shock wave propagates in upstream direction.

Under the assumption of a known adiabatic index γ , these ratios lead to the Mach number

of the shock front. Considering shocks in a monoatomic gas, the adiabatic index becomes $\gamma = 5/3$. This leads to the Rankine-Hugoniot Jump Conditions, where an explicit derivation oriented on (Longair, 2011, 314) is given in B.2.

$$\frac{p_2}{p_1} = \frac{2\gamma M^2}{\gamma + 1} = \frac{5}{4}M^2 \quad (1.7)$$

$$\frac{\rho_2}{\rho_1} = \frac{v_1}{v_2} = \frac{\gamma + 1}{\gamma - 1} = 4 \quad (1.8)$$

$$\frac{T_2}{T_1} = \frac{2\gamma(\gamma - 1)M^2}{(\gamma + 1)^2} = \frac{5}{16}M^2 \quad (1.9)$$

The Mach number is defined as the ratio of the flow velocity v over the speed of sound c_s of the local fluid, with c_s depending on the phase and temperature of the fluid. Hence, the Mach number is always normalized to the underlying local fluid and can be expressed as:

$$M = \frac{v}{c_s} \quad (1.10)$$

Since shock waves disturb the flows of fluids, it is not easy to calculate its morphological evolution by hand. A unique derivation of the sheer amount of involved particle trajectories makes it nearly impossible. Hydrodynamic simulations help to understand the correlations of the shock's evolution in time and their morphological properties. A closer look is going to be taken in the following Subsection.

1.2.4 Morphology of Shocks in Merging Galaxy Clusters

The morphology of shocks in merging clusters does not only depend on pressure, density or temperature fluctuations, but also on the mass distribution of the merging subclusters (Ha et al., 2018). As illustrated in Figure 1.7, a light DM clump traces a more energetic shock with a larger offset of the X-ray peak compared to a heavier DM clump. Predominantly, ideal head-on collisions produce arc-like shocks, whereas small fluctuations in mass and location originate more turbulent and complicated shocks. The mass distribution of dark matter and baryonic matter shares a center of mass, which is slightly offset compared to its initial position of the potential minimum.

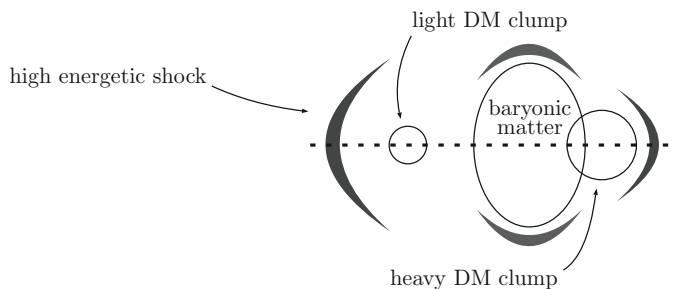


Figure 1.7: Idealized morphology of a head-on merging galaxy cluster. The most energetic and most offset shock from the baryonic matter is in front of the light DM clump along the merger axis.

1.2.5 Radio Relics as an Indication of Shocked Gas in the ICM

Due to the vast distance, pressure jumps of shocked gas in the peripheries of galaxy clusters are hard to detect at most wavelengths. That being said, diffuse radio emissions (also referred to as *radio relics*) are expected to trace shock fronts, thus making them a sufficient indicator of merger shocks appearances (Kale et al., 2017). In this connection, electrons originating from the cosmic radiation emit synchrotron radiation and scatter photons from the CMB to high energies (van Weeren et al., 2019). In most cases, the electrons were accelerated due to Fermi-I acceleration in order to generate these radio relics (van Weeren et al., 2019).²

1.3 Redshift as a Representation of Time

When considering different snapshots, taking different redshifts as representation of time (as displayed in Figure 4.1) can be quite confusing. Intuitively, one would consider a redshift as a measure of a distance, since faraway objects are being increasingly shifted towards longer wavelengths. However, the universe and its cosmology is not just about spacial expansion.

To begin with, the redshift z is defined as the fraction of the difference of emitted and observed wavelengths $\Delta\lambda$, with λ_0 and λ_1 being the initially emitted and observed wavelengths, respectively, divided by λ_0 .

$$z = \frac{\Delta\lambda}{\lambda_0} = \frac{\lambda_1 - \lambda_0}{\lambda_0} \quad (1.11)$$

Following the derivation from (Mukhanov, 2005, 58), a time scaling factor a needs to be worked out due to the expansion of the universe. An expanding universe can be represented by comoving coordinates χ . In this scenario, the source of radiation is at the position of some arbitrary comoving coordinates χ_0 , whereas the observer's location χ_1 is set to 0. A source at χ_0 can emit light of a conformal time difference $\Delta\eta$. The time interval at the moment of emission is not equal to the time interval at the moment of observation, but can be scaled by the factor a , such that following equality holds:

$$\Delta t_0 = a(\eta_0)\Delta\eta \quad \& \quad \Delta t_1 = a(\eta_1)\Delta\eta \quad (1.12)$$

The following relation between λ_0 and λ_1 can be established:

$$\frac{\lambda_1}{\lambda_0} = \frac{a_1}{a_0} \quad (1.13)$$

By inserting this relation in equation 1.11, following expression can be obtained:

$$1 + z = \frac{a_1}{a_0} \quad (1.14)$$

This immediately leads to a strong correlation between redshift z and time t , which enables a sufficient parameterization of time.

²These radio relics can for instance be observed by the Low-Frequency Array (LOFAR) (<https://www.astron.nl/telescopes/lofar/>).

Chapter 2

Methodology

2.1 Magneticum and its Applications

The underlying cosmological, hydrodynamic, n-body simulation for generating the data of merging clusters were carried out using Magneticum (Ragagnin et al., 2016). The simulation *Box2b/hr* was used for this work. It provides an extensive simulation environment, utilizing $5 \cdot 10^{10}$ particles, covering a volume of $(900 \text{ Mpc})^3$ or 640 Mpc h^{-1} . With h being the dimensionless Hubble constant (Schneider, 2006, 11).

$$h = \frac{H_0}{100 \text{ km s}^{-1} \text{ Mpc}^{-1}} \quad (2.1)$$

Detailed parameters of *Box2b/hr* are shown in Table 2.1:

Particles	Size [Mpc h^{-1}]	M_{DM} [M_{\odot}]	M_{gas} [M_{\odot}]	H_0 [$\text{km s}^{-1} \text{ Mpc}^{-1}$]	Ω_m	Ω_{Λ}
$2 \cdot 2880^3$	640	$6.9 \cdot 10^8$	$1.4 \cdot 10^8$	70.4	0.272	0.728

Table 2.1: Parameters of *Box2b/hr*, extracted from the cosmological web portal.

The Web Portal displaying the Magneticum simulation acts like a virtual observatory and offers several services to be chosen from. In the context of this thesis, *Cluster Find* and *SMAC* have been applied, which can be accessed via the web interface (Ragagnin et al., 2016).

2.1.1 Cluster Find

In *Cluster Find*, galaxy clusters are filtered by restricting certain parameters of choice (e.g., mass ranges, temperature, etc.), which can also be divided into subcategories. Additionally, one can decide if the set of interest consists of compact or merging clusters. In this work, a dataset of 1043 merging clusters was extracted as a CSV file, with the set up boundary conditions being shown in Table 2.2.

According to Zhang et al. (2014), strong SZ-X-ray offsets are expected to appear in massive galaxy clusters, so the upper mass boundary for the data set was set to the maximum possible value of $M_{500c} = 1.28495 \cdot 10^{15} M_{\odot}$. Due to density jumps previously mentioned in Subsection 1.2.3 and the X-ray electron density relation (see Subsection 1.2.2), shocked gas also enhances

	$M_{500c} [M_{\odot}]$	$T_{500c} [\text{keV}]$	$L_X [\text{erg s}^{-1}]$	f_{gas}	f_{stars}	Y_{500c}	$M_{\text{sat}}/M_{\text{cD}}$
Min. value	$9.614 \cdot 10^{13}$	1.81	$0.34 \cdot 10^{44}$	0.07	0.02	9.30	0.02
Max. value	$1.28495 \cdot 10^{15}$	11.34	$285.06 \cdot 10^{44}$	0.13	0.04	190.66	1.50

Table 2.2: Constraints for the dataset, which have been used for further analysis.

the surface brightness of galaxy clusters in the shocked regions. Furthermore, dense subclusters are also expected to be involved in strong merger (Zhang et al., 2014). Hence, L_X was also set to its maximum value $285.06 \cdot 10^{44} \text{ erg s}^{-1}$.

2.1.2 SMAC

The service *SMAC* (Dolag et al., 2005) can generate maps of the baryonic density, total mass density, mass weighted temperature, bolometric X-ray luminosity and thermal & kinetic SZ effect. It generates FITS¹ output file, which can be set to an image size from 128 to 4096 pixels. A certain depth can be generated by setting the image z size to arbitrary values in units of kpc. It is possible that a cluster of interest may lay in an unfavorable projection plane, and therefore cannot be used for certain analysis, it is even possible to adjust the projection to any i - j -plane for $i, j \in \{x, y, z\}$, where $i \neq j$. The size factor of the image can be varied from $1 \cdot 2 \cdot R_{500c}$ to $4 \cdot 2 \cdot R_{500c}$. As already reasoned in 1.2.1, the main focus was put on investigating the thermal SZ effect, i.e., Compton- y maps to generate the corresponding pressure maps. Also, bolometric X-ray luminosity maps have been extensively generated, in order to search for correlations in offset X-ray and pressure peaks. While executing every single job separately - considering a dataset of 1043 galaxy clusters - can be exhausting, it is possible to execute any Web Portal service via the command line, thanks to Antonio Ragagnin's² code `C2PAP_BATCH.PY`. The code requests jobs, let these jobs be calculated by the Web Portal and downloads executed jobs to a specified directory autonomously. This makes it a very efficient method to request SMAC maps for vast datasets.

2.2 Extracting Physical Values from FITS Files

Similar to TIFF, JPEG or PNG files, FITS images are bitmaps consisting of pixels. Every pixel is assigned to a certain position in the grid and hosts certain values, e.g., representing colors. In contrast to the aforementioned data types, FITS files do not store color values per pixel, but real physical values, for instance the Compton- y parameter for a determined coordinate in the bitmap grid. In Figure 2.1, a typical FITS file is illustrated.

Since bitmaps are numerical values stored in arrays, they can be interpreted by most programming languages. The Python module *Astropy*, which was used in most of this work's codes, is amongst other things laid out to interpret FITS files. The pixel values of these images are imported as a matrix. Aside from the pixel values, other information, e.g., the converted pixel size to physical values or coordinates of the portrayed cluster, can be stored in so-called *headers*.

¹<https://fits.gsfc.nasa.gov/>

²<https://aragagnin.github.io/>

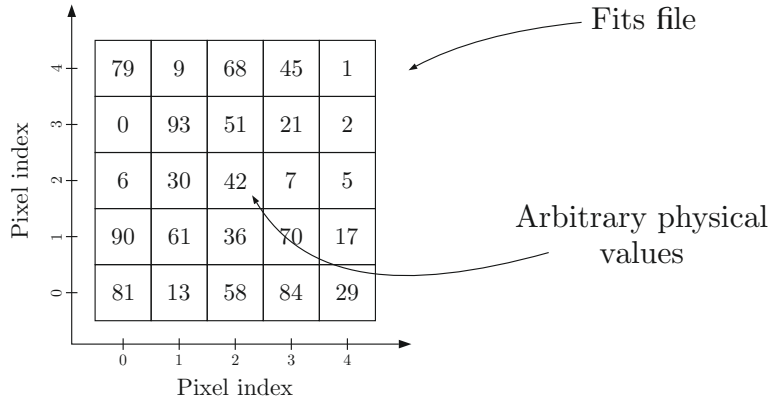


Figure 2.1: Illustration of a FITS file. Every pixel hosts a certain physical value and can be identified by its coordinate.

2.2.1 Calculating Distances

Since every cluster has its own unique radius, it is crucial to extract distances of these images which are normalized to a certain parameter, such that distances from different clusters can be brought into context. This becomes handy when offsets of certain clusters need to be compared to each other. A normalized distance d_n from any cluster can be calculated by simple geometrical considerations. First, the distance in units of pixels needs to be calculated by the pythagorean theorem. As every pixel is indexed by its x and y position, their positions can be understood as two dimensional vectors in the x - y -plane. Here, the absolute value of the vector \vec{d} , connecting the center and the position of the desired pixel, is calculated as follows:

$$|\vec{d}| = \sqrt{x^2 + y^2} \quad (2.2)$$

An example is shown in Figure 2.2: The desired pixel is offset from the center by 2 pixels in x -direction and 1 pixel in y -direction, which results in a total distance of $|\vec{d}| \approx 2.24$.

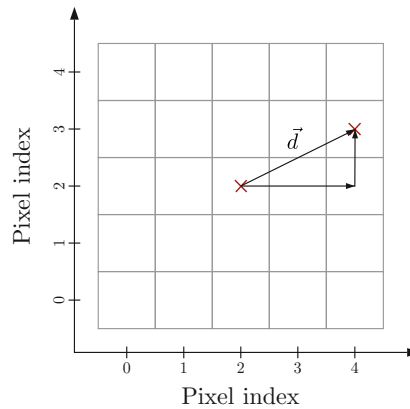


Figure 2.2: Calculating distances in bitmaps.

Starting from $|\vec{d}|$ in units of pixels, its physical distance can be obtained by multiplying $|\vec{d}|$ with the physical pixel size p_{phy} . In this case the physical pixel size will always be in magnitudes of kpc. In order to obtain distances irrespective of the different galaxy cluster sizes, r_{500c} can be used to normalize the calculated physical distance. Since r_{500c} can individually be extracted from the FITS header files, a global normalized distance d_{norm} can be expressed as

$$d_{\text{norm}} = \frac{|\vec{d}| \cdot p_{\text{phy}}}{r_{500c}} \quad (2.3)$$

2.2.2 Measuring Distances and Physical Values with *SAO Image DS9*

Generated FITS files can be post-processed by several imaging tools - for astronomical purposes, however, it is common to use the program *SAO Image DS9*³ (see William Joye (Smithsonian Astrophysical Observatory)). It does not only find use in post-processing telescope images, but also plays a significant role in extracting physical data and enhancing scientific interpretations from images. In this manner, offsets of shocks and other data peaks starting from the image's center were measured.

In order to obtain the distance, a circle was drawn at the center of the image. With its edges touching the shock front, the radius can be extracted from this region by a simple command. The radius still needs to be normalized by applying the method from 2.2.1. If one for instance would measure the distance the shock propagated over time, $r(z_1)$ and $r(z_2)$ can be extracted from the radii via DS9 (see Figure 2.3). In this example the values are extracted from the snapshots showed in Figure 4.1 at redshifts $z_1 = 0.29$ and $z_2 = 0.25$:

$$r(z_1) = 109.93 \text{ pixels} \stackrel{(2.3)}{\approx} 0.47 R/r_{500c} \quad (2.4)$$

$$r(z_2) = 249.70 \text{ pixels} \stackrel{(2.3)}{\approx} 1.11 R/r_{500c} \quad (2.5)$$

with its physical pixel size at redshifts $p_{\text{phy}}(z_1) = 4.50 \text{ kpc}$ and $p_{\text{phy}}(z_2) = 4.70 \text{ kpc}$ with $r_{500c}(z_1) = 1047.66 \text{ kpc}$ and $r_{500c}(z_2) = 1060.44 \text{ kpc}$. Hence, the shock propagated in Δz over a distance of:

$$\Delta r = r(z_1) - r(z_2) = 0.64 R/r_{500c} \quad (2.6)$$

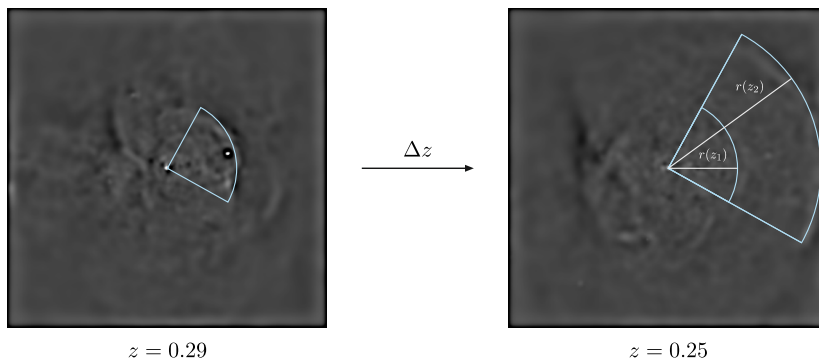


Figure 2.3: Measuring the distance of a shock propagating through space over time with DS9.

It shall be noted, however, that distances of surface brightness peaks or centroids have been automatically calculated by a written python code. Measuring the distances in all of the clusters by hand would not only be time-consuming, but also increase the measurement uncertainty.

³<https://sites.google.com/cfa.harvard.edu/saomageds9/home>

2.3 Radial Binning

Looping the iterations of d_{norm} using python enables to calculate every distance of every pixel with very little effort. Since every pixel is still storing real physical values (e.g., the Compton- y parameter), radial profiles starting from the center can be obtained. Generating radial profiles out of bitmaps originates from the common method of kernel density estimation. Here, all pixels within a certain distance range are binned, which produces a histogram of counted pixels. However in this manner it is not of interest by counting how often a pixel is detected at a certain distance, rather knowing what pixel values are how often related to a certain distance. Using the counted pixel values at certain distances, allows to calculate the mean physical value at the related d_{norm} . In Figure 2.4 an illustration about the binning process is given in three different steps: first, the distributed pixel values are divided into four different bins (indicated by the dashed lines). Then, the mean pixel value is taken, such that the distributed values are represented by a horizontal line in each bin. Starting from the distribution of the horizontal lines in the last step, the best fitting curve is being drawn through the center of each line, such that it optimally fits the distributed pixel values.

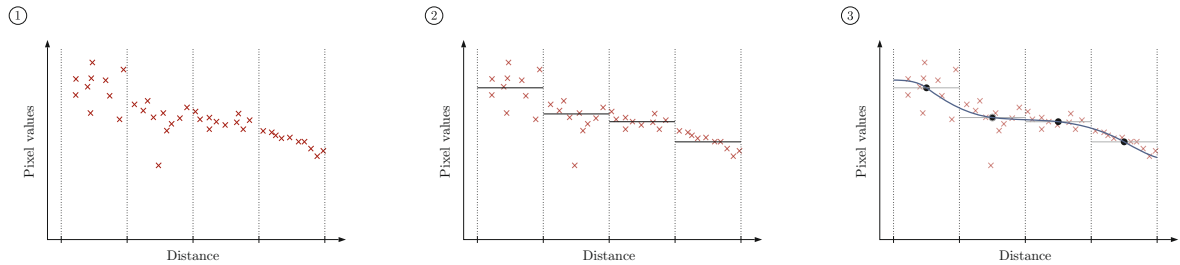


Figure 2.4: Radial binning of a FITS file. The dashed lines mark the boundaries of every bin. Hence, in total there are four bins. In every bin there are different pixel values distributed in a certain range.

This method of extracting physical values over a certain region is a common tool in astrophysics in order to get an idea how certain properties evolve over a given distance. Radial profiles do not necessarily need to be extracted by averaging over a whole circle domain - it is also possible to investigate small circle segments defined over a certain polar angle. In this work, however, profiles were only taken from a fully enclosed radial parameterization. In the upcoming chapter, the evolution of physical properties over a certain distance is presented.

2.4 Gaussian Filtering

Gaussian filtering is an imaging process, where pixels are smoothed by taking the weighted average of values in a local region. The strength of the filtering gradient at a certain position is determined by the two dimensional Gaussian function (Burger and Burge, 2016, 98):

$$G(x, y) = \exp \left[-\frac{x^2 + y^2}{2\sigma^2} \right] \quad (2.7)$$

Starting from the center of the picture, i.e., at the pixel indices $(257, 257)$, the bell shaped function “travels“ over the image at distances of increasing radii $r = \sqrt{x^2 + y^2}$. The standard deviation is represented by σ and can be chosen as a parameter in the code. For the analysis, $\sigma = 5$ was used. The maximum averaging weight is assigned to the pixel at the center of the bell-shaped function.

Now the question may arise, why especially this type of image processing becomes handy for these astrophysical purposes. Since, the picture is smoothed by the pixel value weights, the filter needs to average over a larger local region, if one pixel differs by a larger gap from another pixel. As the three-dimensional plot in Figure 2.5 illustrates, the Gaussian filter lifts a lot more pixels to higher values at the center, since the value gradient from the almost seeming δ -peak pixel from the original image stands out in comparison to its surrounding pixels. Now, the plot filtered by the Gaussian may connote a large pixel value lift in general, but this does not hold true for this particular case (see z -axis ticks), which means that the thin peak from the original picture is attenuated by a certain factor.

In order to obtain a difference in the pixel gradients, the Gaussian image Im^{Gau} needs to be subtracted from the original one Im^{Ori} and further be divided by the Gaussian picture again. The final reduced Gaussian image Im^{Red} is given by:

$$\text{Im}^{\text{Red}} = \frac{\text{Im}^{\text{Ori}} - \text{Im}^{\text{Gau}}}{\text{Im}^{\text{Gau}}} \quad (2.8)$$

This method produces the desired difference image with respect to the initial pixel value. In this case, a relative pressure map is being generated from a Compton- y map.

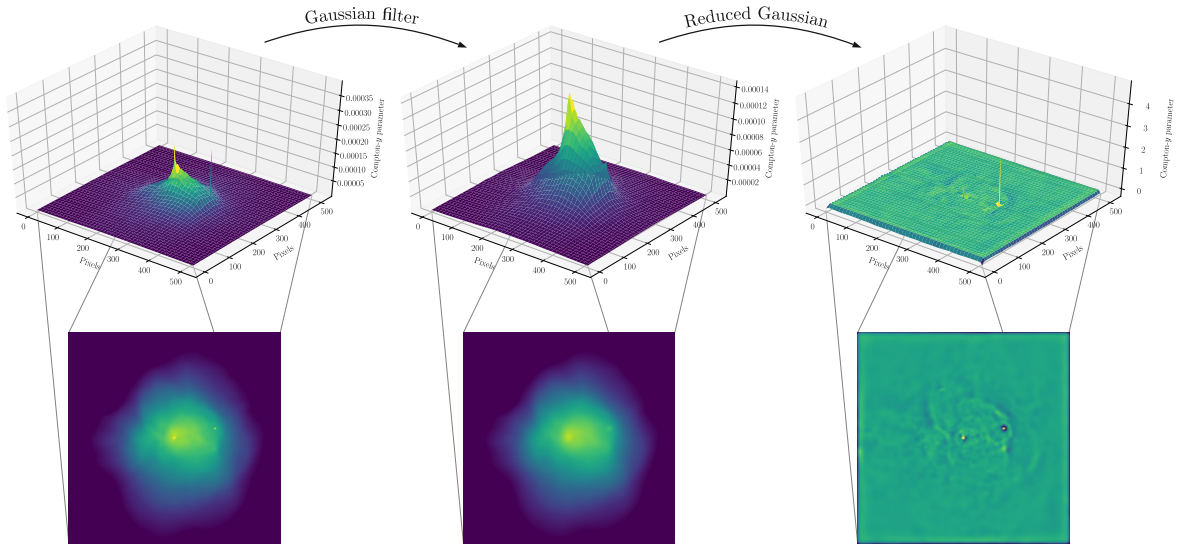


Figure 2.5: Gaussian filtering process of cluster number 65 at redshift $z = 0.29$. The Compton- y parameter is color-coded from blue to yellow for increasing values.

Chapter 3

The Offset of SZ and X-ray Positions in Merging Clusters

3.1 Constellations of Shock Morphologies

Within the cluster PLCK G200.9-28.2, a relative offset of 700 kpc between the SZ position and the cluster’s X-ray peak was detected by Kale et al. (2017). SZ and X-ray signals were measured by the Planck satellite and the XMM-Newton observations, respectively, and led to the suggestion that the offset originates from a physical process, i.e., a merger. Hence, the dataset of simulated clusters for this thesis was restricted to substructures, i.e., member galaxies, which subject to an ongoing merger. This dataset accommodates 1043 galaxy clusters and is described in more detail in Table 2.2. By applying a Gaussian filtering process (see Section 2.4) to all of the cluster’s FITS files, occurring shocks can be made visible. Looking through the generated relative pressure maps via *SAO Image DS9*, the set of clusters hosting shocks was worked out.

Merger shocks	Shock halos	Not categorizable	No shock
11.22%	7.67%	7.09%	73.92%

Table 3.1: Morphological distribution of detected shocks from the dataset consisting of 1043 merging clusters.

In this work, merger shocks have been considered as shapes with at least a single arc-like pressure jump detection (double arc-like shocks count as merger shocks as well). These appearances should occur perfectly in the observer’s plane, whereas single shocks may be caused by an unfortunate merger geometry (Kale et al., 2017). Due to the merger’s equatorial shocks, shock halos may occur whenever the merger axis points perfectly towards the observer’s direction. The shocks appear to be projected as rings around one central cluster. However, there have been plenty of clusters where either shocked gas has been detected, but could not be adequately identified as a shock wave, or none of observable merger outcomes have been detected (the latter has been classified as *No shock*). Some example data is shown in Figure 3.1. In some cases, it is hard to distinguish to which category a cluster belongs, since axis projections may cause different kinds merger morphologies.

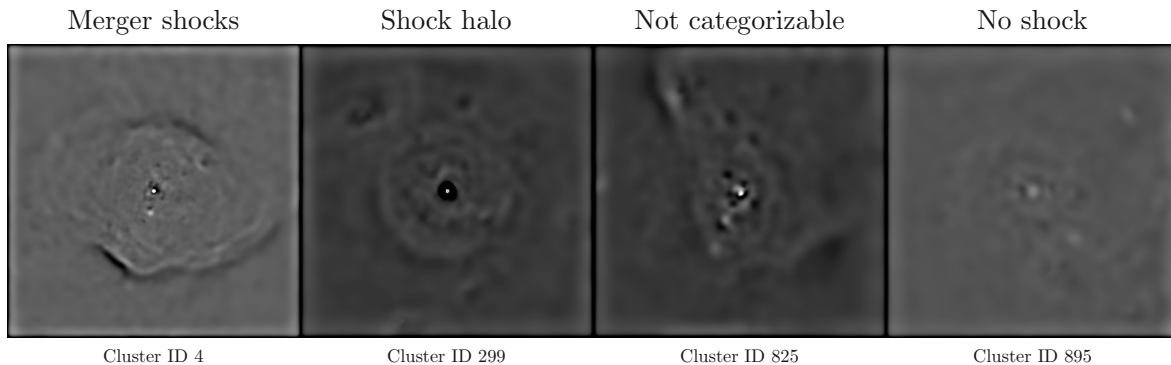


Figure 3.1: Example clusters for assigned categories.

3.2 Comparison of SZ-X-ray Peak Offsets of Simulated Clusters to the Observed Cluster PLCK G200.9-28.2

Since the SZ peak is proportional to its pressure (see Equation 1.5) and the X-ray surface brightness is generally representing high electron densities due its n_e^2 proportionality (see Equation 1.6), Kale et al. (2017) suggested that an SZ-X-ray offset could indicate a merger. The SZ peak should trace the shock wave and the X-ray peak remains at the densest regions in the cluster. Hence, the distance of the SZ peak relative to the distance of the X-ray peak was investigated in the sample data of detected merger shocks, which scored a total amount of 117 out of 1043 clusters. To obtain proper positions of the SZ and X-ray peaks, again a Gaussian filter was applied to the raw FITS files in order to smooth the transitions and get rid of small, but strong brightness artefacts unrelated to the merging subclusters. In this case, σ was set to a value of 20. Some of the simulated mergers reproduced the researcher's reported scenario quite well (see Figure 3.2), however, the SZ-X-ray offset in the cluster shown in Figure 3.2 (ii) is significantly weaker, compared to the observed cluster PLCK G200.9-28.2. The simulated SZ-X-ray offset amounts to ~ 226.68 kpc, whereas the observed offset was reported to extend up to 700 kpc. The dominant shock of cluster 479 reaches a width of ~ 36.33 kpc and a maximum length of ~ 333.13 kpc. This shock sizes 12.98% in width and 32.66% in length in comparison to the cluster's PLCK G200.9-28.2 radio relic.

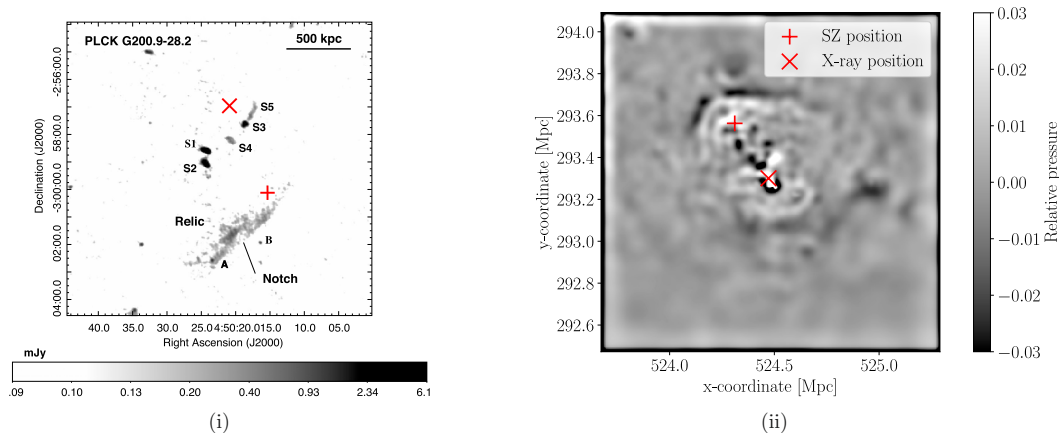


Figure 3.2: Comparison of (i) the reported cluster (PLCK G200.9-28.2) by Kale et al. (2017), observed by the Giant Metrewave Radio Telescope (GMRT) in the 610 MHz spectrum, to (ii) the simulated cluster (Cluster ID 479). Both host a shock in the cluster's periphery. In (i) and (ii), the SZ and X-ray peaks are marked as + and \times , respectively. However, the SZ-X-ray offset, as marked in (ii), is a lot smaller than in (i).

In Figure 3.3 a closer look was taken into the radial profiles of the SZ, X-ray and relative pressure maps, respectively. The dashed annotations mark where each peak is located. By comparing the SZ and relative pressure profiles one can see a relatable steepening in a region, right after their peaks. Indeed, this similarity may indicate that the SZ distribution traces the shock wave. Since the radial profile was calculated over an angle of 360° , a larger pressure plateau, ranging from approximately $7 \cdot 10^{-2}$ to $10^0 R/r_{500c}$ is assignable to both shocks in Cluster 479. The lowest value in the relative pressure profile marks the boundary in between the two shock fronts - also visible in Figure 3.2 (ii) - quite well. In the radial X-ray profile, it is noticeable that the X-ray peak is oriented towards the highest mean X-ray values. As a result, this supports the suggestion, that the densest region and therefore also the X-ray peak is generally located towards the cluster's center.

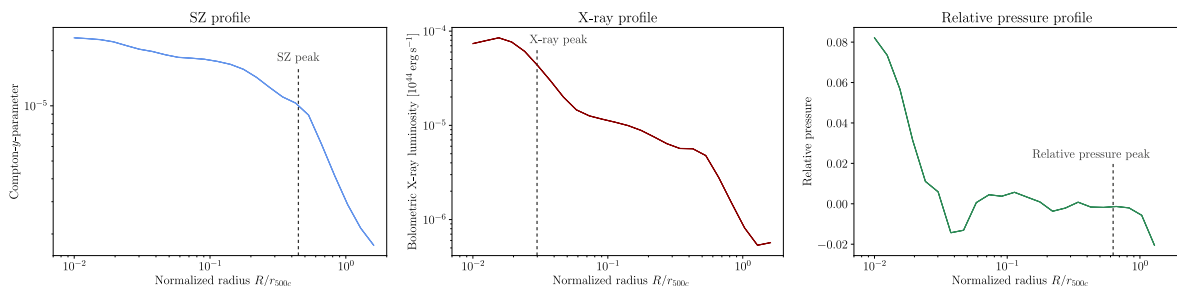


Figure 3.3: Radial profiles of Cluster 479.

Statistical analyses show how often this particular SZ-X-ray offset scenario occurred, as shown in Figure 3.2. In Table 3.2, the distribution of multiple SZ-X-ray combinations is given:

Properties	A	B	C	D
Proportion	17.09%	8.55%	17.09%	57.26%

Table 3.2: Distribution of SZ-X-ray offset combinations. In this Table A, B, C and D are labelled as *SZ peak in shock direction*, *X-ray peak in shock direction*, *SZ & X-ray peak in shock direction* and *No correlation*, respectively.

The largest offsets, however, have been detected where the subcluster hosting its SZ peak is not the only object tracing a shock wave or being offset from the barycenter. In these cases, the subcluster hosting the X-ray peak is representing the bullet, whereas the SZ-Peak is related to the more massive subcluster, also representing the target (this distribution is suggested by Zhang et al. (2014)). According to their investigations, an X-ray peak mainly corresponds to the densest gas region, belonging to the smaller subcluster, on the other hand the SZ peak is rather oriented towards the larger subcluster, i.e., the center of mass. This explains why, in some cases, SZ-peaks found towards the inner regions do not necessarily correspond to a shock (see Cluster ID 918 in Figure 3.4). Cluster 461 and 918 both host the largest SZ-X-ray offset of the sample data of detected shocks, amounting to 304.09 kpc and 299.24 kpc, respectively (see Figure 3.4).

Even for the most extreme cases, such a large offset as reported by Kale et al. (2017) could not be found in this dataset. However, the distances in the extracted FITS files are projections of a three-dimensional cluster, mapped onto a two-dimensional plane - hence, distances of different subclusters of brightness peaks can be distorted due to projection effects (see Figure 3.5). Therefore, the extracted results highly depend on the orientation of the collision axis

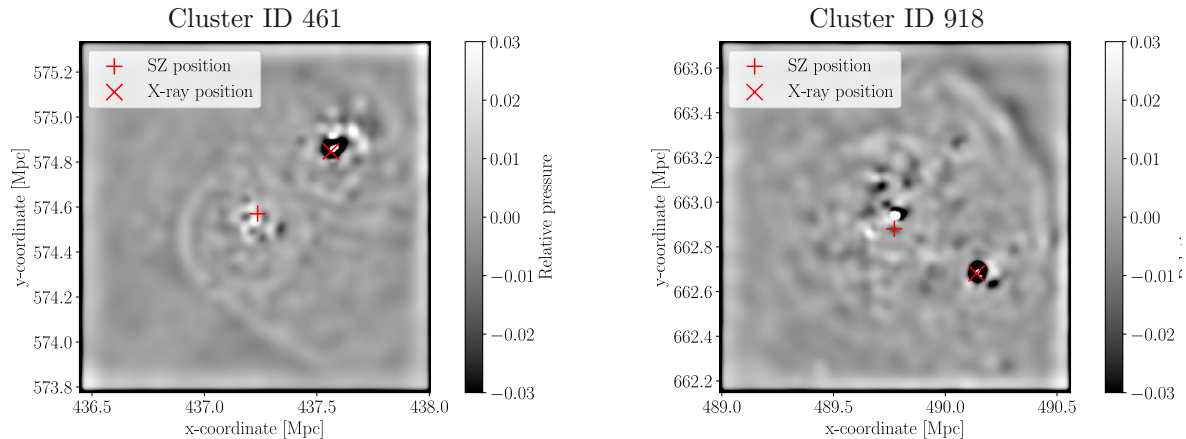


Figure 3.4: Centered SZ signal peak and offset X-ray peak.

with respect to the projection plane. Considering the dataset of detected shocks, it is unlikely to obtain a collision scenario with its collision axis being perfectly oriented parallel towards the projection plane. It is believed that most cluster collisions end up in an orientation similar to (ii) in Figure 3.5, which, in almost every case, causes a decrease in the distance of the separated SZ and X-ray peaks. According to the pythagorean theorem, a three-dimensional distance is always greater or equal to its two-dimensional projection.

$$r_{2D} = \sqrt{x^2 + y^2} \leq \sqrt{x^2 + y^2 + z^2} = r_{3D} \quad (3.1)$$

With z being the cluster's depth perpendicular to the projection plane (if $z = 0$, a perfect projection exists). In consideration of the projected offsets it should be noted that the obtained distances are probably shifted towards lower values. However, the distribution shape of the offset should still remain a statistically sufficient representation, since the initial positions and the corresponding velocity orientations of the subclusters are evenly distributed. Subfigure 3.5 (ii) could also explain why some of the shocks have a broader opening angle, even if their location is close to the barycenter. Indeed, the shock wave could propagate over a greater distance and would have been able to spread into space over time. This creates the illusion of large shocks occurring almost in the center of mass.

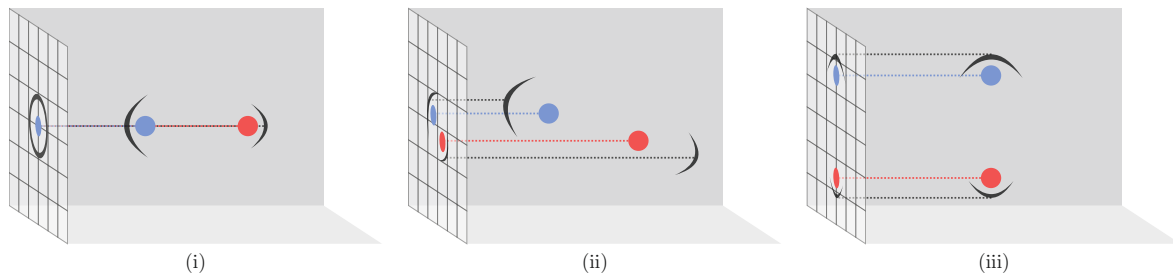


Figure 3.5: Three kinds of appearances of different projection scenarios, which occur when a three-dimensional collision is mapped onto a two-dimensional plane. Here, (i) is a perpendicular projection, (ii) is a slightly shifted projection and (iii) is a parallel projection relative to the collision axis. The blue and red spheres can either represent SZ or X-ray peaks, as already discussed previously.

3.3 Investigation of SZ and X-ray Centroids

In order to determine whether an appearance of shocks and an SZ-X-ray peak offset correlate, the number of certain offset occurrences and their corresponding displacements have been studied (see Figure 3.6 (i)). The analysis was carried out for the sample of detected shocks (*Sample 1*), and a sample of no shocks detected, containing the same amount of clusters (*Sample 2*). By considering the distribution of the counts and the corresponding distance of measured offsets, no significant difference could be found. A slight increase of the normalized SZ-X-ray mean offset was calculated for the sample data of detected shocks in comparison to the dataset, where no shocks were detected (the mean offsets, however, only differ in the third decimal place). Similar circumstances hold for Subfigure 3.6 (ii), where the SZ-X-ray displacements were extracted by calculating the surface brightness centroid peaks. The displacement range in (ii) was expected to be a lot smaller than in (i), since SZ and X-ray signals come from emissions of baryonic matter. As already discussed in Section 1.2.4, a general centering of baryonic matter, closer to the more massive subcluster, takes place. Hence, calculating the SZ and X-ray centroids would only result in small displacements relative to each other and offsets from the center of mass.

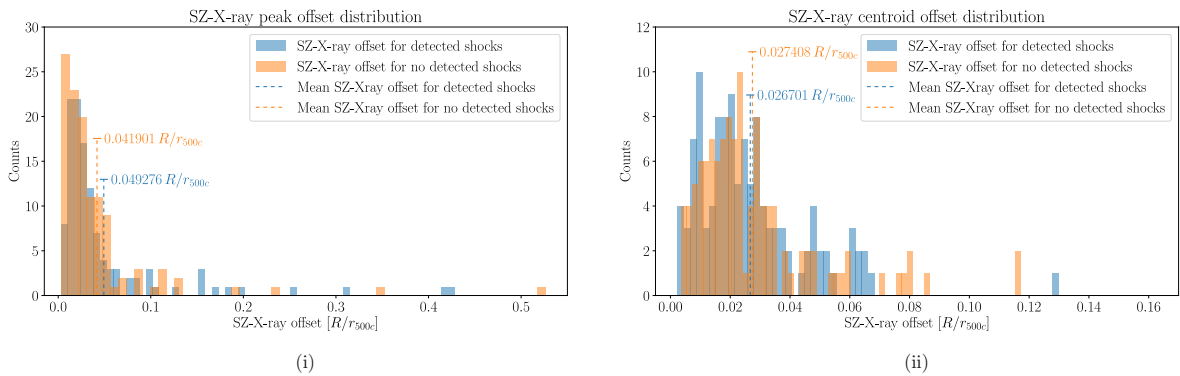


Figure 3.6: Histogram of the distribution of SZ-X-ray displacements in units of the physical radius, normalized by r_{500c} . The clusters with detected shocks are labelled in light blue, whereas clusters hosting no detected shocks are colored in orange. The histogram in (i) was taken by considering only the surface brightness peaks. (ii) displays the same samples, however taken the emission centroids from the SZ and X-ray surface brightnesses.

Considering the small difference of the mean SZ-X-ray displacements of detected and no shocks, it could be possible that this circumstance may occur, because shocks dissipate energy and hence steepen their relative pressure over time. A shock can disappear from pressure maps once its energy gets under a certain threshold. Because both datasets were only hosting merging clusters showcasing more or less the same disturbances of subclusters, it might be justifiable that - concerning the dataset without detected shocks - most of the strong pressure jumps already disappeared over time. Hence, merged subclusters could have been decelerated enough to justify an average movement towards the potential minimum of the cluster took place. This could cause the slight decrease of SZ-X-ray offsets in clusters, where no shocks have been detected. Since DM only interacts weakly with baryonic matter, if at all (Chan, 2019), it could be conceivable that this statement of merging evolution could be supported by investigating the total mass density distribution. By considering clusters with detected shocks, one could expect the centroid of the total mass density to be closer towards the potential minimum than in datasets without shocks. In this case, it is assumed that - compared to baryonic matter clumps - DM cores are less efficiently decelerated while the merger proceeds, which would result in a larger total mass density centroid offset relative to the center

of gravity of the most massive subcluster. On the other hand, some initial velocities of subclusters could have been too low for generating strong enough pressure jumps in order to form a shock wave, which could be suggestive of mass distributions of subclusters existing in the peripheries. However, it is more likely that the merger was not strong enough, and the general mass distribution is similar to the SZ and X-ray distribution shown in Figure 3.7 (ii). Further investigations regarding this topics are taken in the next chapter.

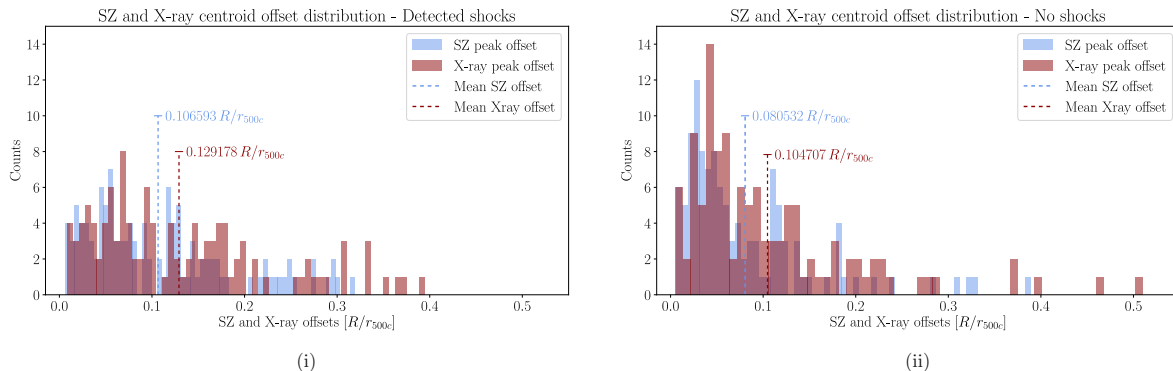


Figure 3.7: Histograms of the SZ and X-ray centroid offset distributions. In (i), the distribution was extracted from the dataset, where shocks have been detected, whereas in (ii), the dataset hosting no shocks was taken into account.

In order to check whether the SZ or the X-ray peak is more oriented towards higher mass subclusters, additional histograms (see Figure 3.7), with the surface brightness centroid offset being calculated relative to the cluster’s center of mass, were generated. The mean SZ offset is roughly 20 – 30% more shifted towards the center of the most massive subcluster in comparison to the X-ray centroid, a trend which can be observed in both datasets. This significant separation indicates quite clear that X-ray centroids have a stronger correlation to distant shock waves validating an association with a bullet merging through a target (Zhang et al., 2014). By comparing (i) and (ii) of Figure 3.7, it can be observed that the offset distribution in the dataset of detected shocks is spread out slightly wider within the range of 0 to $0.4 R/r_{500c}$, compared to Subfigure (ii). This could indicate that most of the subclusters are still subjected to the ongoing merger and tend to be located towards the cluster’s peripheries. The general decrease of the mean offsets of SZ and X-ray centroids in (ii) could also point towards subclusters not having enough kinetic energy to reach further distant regions in the cluster’s peripheries. Besides investigating the total mass density distribution, a larger dataset would either confirm or refute this statement. However, generating significantly larger datasets than 1000 clusters would occupy a lot more computation time and would go beyond the scope of this work.

To validate the distribution of the simulated X-ray centroids by Magneticum a comparison with observational data provided by Yuan and Han (2020) was investigated. Considering this data, the researches had to define a centroid shift ω , which determines the X-ray peak offset relative to the emission centroid. That has lead to the following definition (Evrard et al. (1993); Poole et al. (2006); Maughan et al. (2008)):

$$\omega = \frac{1}{R_{\text{ap}}} \left(\frac{1}{N-1} \sum_{i=1}^N (\Delta_i - \langle \Delta \rangle)^2 \right)^{1/2} \quad (3.2)$$

With R_{ap} , Δ_i and $\langle \Delta \rangle$ being the aperture, the distance between the X-ray peak and the center

of the i th aperture and the mean centroid of the cluster emission, respectively.

In contrast to the observational data, Magneticum uses subfind algorithms in order to determine where the center of the most massive subcluster is located (Dolag et al., 2009). Therefore, instead of using the definition of ω given in Equation 3.2, only the centroid shifts relative to the potential minimum of the most massive subcluster were taken.

The ω values calculated by Yuan and Han (2020) were extracted from *Table 1*¹. In this Table the first 117 (amounting to the same sample size as the simulated dataset) clusters with a given ω were taken into account. The observational data consists of 964 galaxy clusters archived by the Chandra X-ray Observatory.² In order to match the scaling with the data from Magneticum, the logarithmic values had to be transformed into linear values. Figure 3.8 monitors a comparison of the observational and the simulated data. In Subfigure 3.8 (i) a histogram of the centroid shift from the observed data and the data of *Sample 1* was plotted, whereas in Subfigure 3.8 (ii), *Sample 2* was taken into account. In both plots the mean simulated centroid shift extends to a larger distance than the observed one. However, this consequence originates from the initial constraint that only merging substructures have been considered in the simulated dataset, whereas the observational data consists of dynamically relaxed and merging subclusters. It stands out that the centroid difference of observed and simulated data $\Delta\omega$ from *Sample 1* amounts to a larger value of $\Delta\omega_{S1} \approx 0.076 r/R_{\text{ap}}$ than from *Sample 2*, amounting to $\Delta\omega_{S2} \approx 0.021 r/R_{\text{ap}}$. This points out the strong correlation of the dynamical state of a galaxy cluster and its centroid shift, since a large $\Delta\omega_{S1}$ was expected, considering the initial constraints.

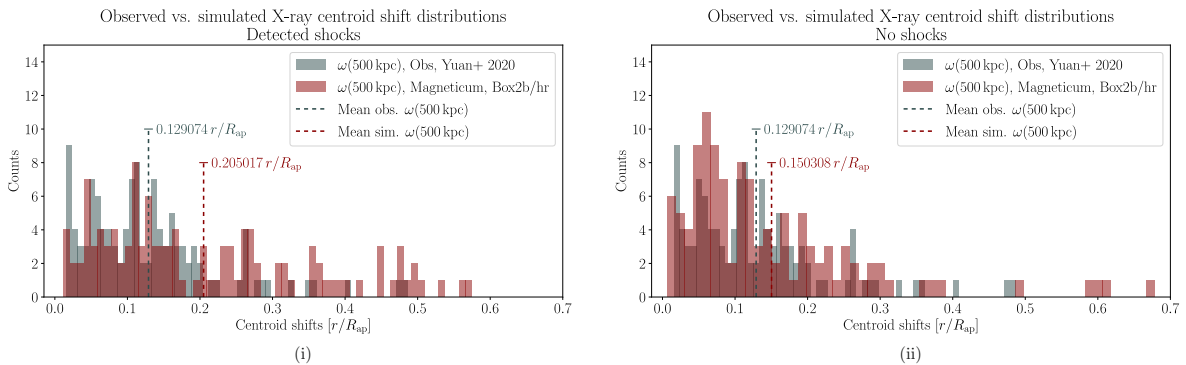


Figure 3.8: Comparison of the by Magneticum simulated and the observed centroid shift ω provided by Yuan and Han (2020). In Subfigure (i) *Sample 1* was compared to the observations, whereas *Sample 2* was investigated in Subfigure (ii).

¹http://zmtt.bao.ac.cn/galaxy_clusters/dyXimages/

²<https://cxc.cfa.harvard.edu/>

Chapter 4

The Offset of Total Mass Density Positions in Merging Cluster

4.1 Morphological Evolution of Mass Distributions over Time

In order to analyze the mass distribution of the subcluster regarding the SZ and X-ray offsets, the merger constellation as discussed in Section 1.2.4 needs to be confirmed in order to be reproducible. Therefore, a closer look was randomly taken at a cluster (Magneticum Cluster ID 65), extracted from the Table of detected shocks in merging clusters A.1. Here, the cluster is illustrated at four different stages of redshifts, which include the cluster's relative pressure, the Compton- y -parameter, the X-ray luminosity and the total mass density respectively (see Figure 4.1). Considering redshift $z = 0.34$, the left subcluster can be identified as the bullet colliding with the more massive target, which is represented by the centered, bright peak. At redshift $z = 0.29$, the lighter subcluster has passed the central subcluster and traces a strong shock. At the redshifts $z = 0.29$ and $z = 0.25$, the total mass density displays very well how much the light DM clump is offset from its target. As already motivated in Section 1.1 this merger appearance is relatable to the so-called Bullet Cluster. Indeed, a merger process similar to the Bullet Cluster was reproduced by Mastropietro and Burkert (2008). It can be concluded that the bullet remains mostly as dark matter, since as well as in the Compton- y as in the X-ray maps, no brightness peaks can be located anymore, where the total mass peak is expected. Considering the surrounding, randomly distributed shocks, one can conclude that the merger was not perfectly head-on, yet still reproduces the expected morphologies evolving over time.

4.2 Distribution of Total Mass Density Offset Centroids

By considering the counts of the total mass density (TMD) offset distribution, the difference of *Sample 1* and *Sample 2* is still recognizable (see Figure 4.2). In these histograms, the counted mass distributions follow a similar shape as the SZ and X-ray centroid offset distributions (see Figure 3.7), as well as in *Sample 1* as in *Sample 2*, where the mean TMD offset is lower than the mean SZ and X-ray offsets. This may lead to a confusion, because a strong separation is obviously noticeable in Figure 4.1. It should be noted that - even if a strong separation of subcluster mass distributions is detectable - the surviving bullet is by far lighter than the target. Hence, the calculated centroid of the TMD distribution would be shifted towards the lower potential of the whole galaxy cluster, which leads to a decrease in the mean barycenter offset

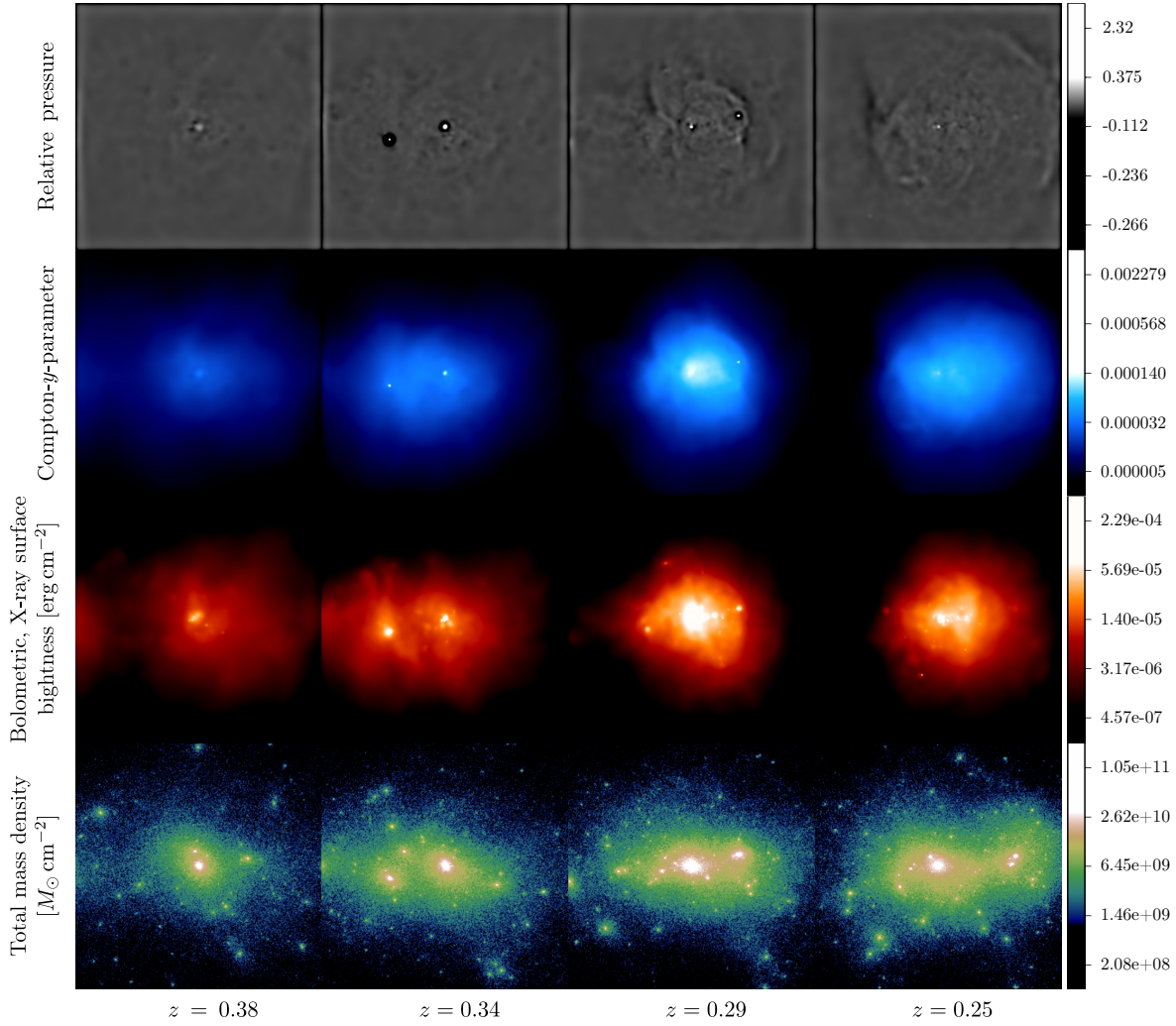


Figure 4.1: Ongoing merger at four different states from $z = 0.38$ to $z = 0.25$. The direction of the shock and morphology can be extracted from the relative pressure frames, whereas the Compton- y and the X-ray maps illustrate offset brightness peaks and the total mass density mainly traces the DM clumps.

of the merging subclusters. In Subfigure 4.2 (ii), most counts are slightly oriented towards the cluster's barycenter, and only a few are located at high offsets. This supports the statement that *Sample 2* could mainly host merging clusters which do not have the desired initial kinetic energy to form shock waves. The few counts in the range of 0.25 to $0.3 R/r_{500c}$ could indeed be identified as subclusters, which initially formed shocks and dissipated later. On the other hand, it could be possible that clusters have been mistakenly assigned to *Sample 2*, because the shocks are located way beyond the range these FITS files can display. The TMD offsets of *Sample 1* are similar to the SZ and X-ray peak offsets more evenly distributed over distance. However, the distribution range is better comparable with the distribution range of the X-ray offset peaks - especially regarding the similarity of their distribution shapes, which points towards a correlation of an SZ-X-ray-TMD scaling. This is investigated in the following Section.

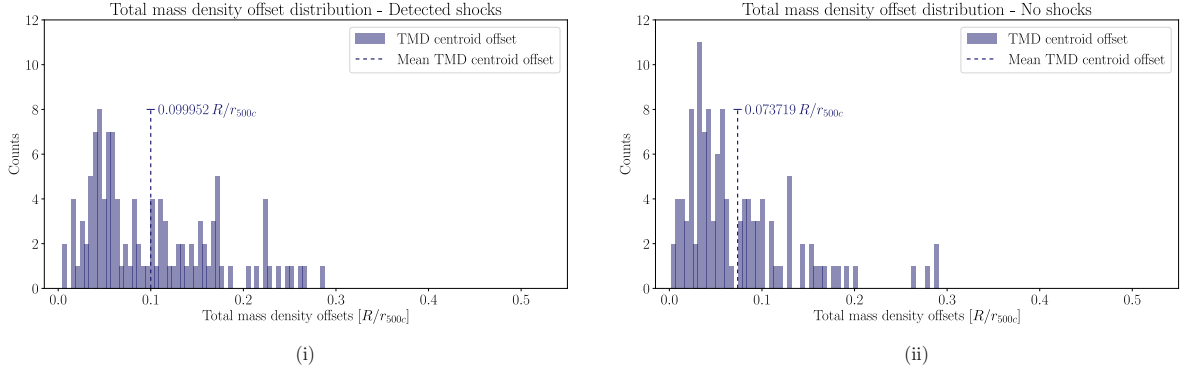


Figure 4.2: TMD centroid offset distribution of *Sample 1* (i) and *Sample 2* (ii). The mean offset in (ii) shows a slight decrease, amounting to approximately 2.6% in distance in comparison to (i).

4.3 Correlation of SZ, X-ray and TMD Offsets

Finally, the possible correlation between clusters hosting shocks and the SZ, X-ray or TMD centroid offset peak distributions, as well as relation between the SZ-X-ray offset and its distance relative to the barycenter of the cluster, were investigated. First, the SZ-X-ray displacement related with single SZ or X-ray offset were examined, as a potential relative distance increase for further distant SZ or X-ray peaks due to the proceeding merger dynamic was previously suggested. In Figure 4.3, *Sample 1* and *Sample 2* were plotted in blue and orange, respectively. In (i), the x -axis represents the SZ centroid offset, whereas in (ii), the X-ray centroid offset is plotted. In detail, large SZ-X-ray signal offsets can be coequally detected - at small offsets as well as at the distant peripheries of the galaxy cluster. It should be noted, however, that only the centroids were considered, since bright subclusters not belonging to the merger could occur and possibly distort statistical results. By taking the brightness center of both signals, it becomes apparent that SZ-X-ray displacement fluctuations could only differ in the range of 0 to $0.14 R/r_{500c}$. It shall be noted that the second plot derives from the first one, however, it still showcases the underlying properties if only the X-ray spectrum can be experimentally observed.

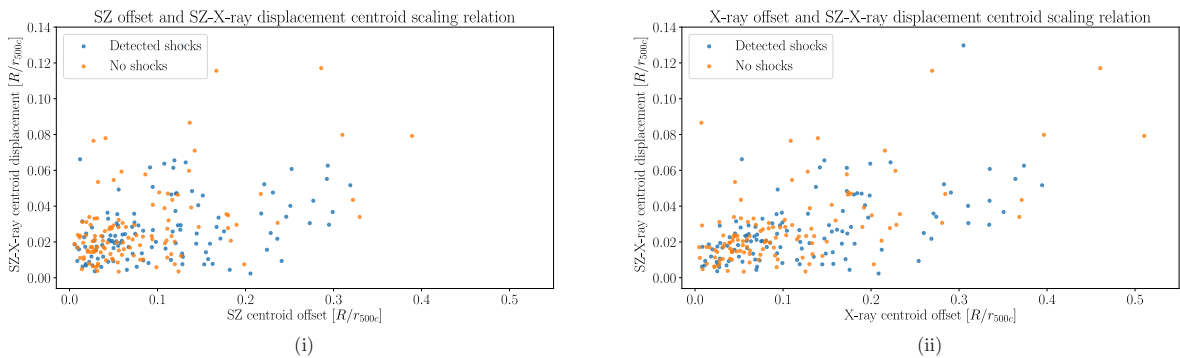


Figure 4.3: Scatter plot of (i), the SZ centroid shift and SZ-X-ray displacement, and (ii), the X-ray centroid shift and SZ-X-ray displacement. In the small SZ-X-ray range of 0 to $0.14 R/r_{500c}$, both plots show strong displacement fluctuations.

Taking into account every cluster from *Sample 1* and *Sample 2*, the respectively matching peaks in surface brightness and mass were extracted and scatter-plotted in order to see if the distance of any offset scales with the other two. In Figure 4.4, the X-ray centroid offset peaks are plotted against the SZ centroid offset peaks, with the TMD centroid shift color-coded

from yellow to violet for increasing distances. It is unambiguously that all of the offsets correlate to each other in both samples. It can be unequivocally stated that all of the offsets correlate with each other in both samples, which means that if an offset detected from the SZ effect relative to the barycenter of the clusters is detected, also an offset of the X-ray surface brightness offset (and vice versa) can be expected on a linear scale. Thus, the separation of subcluster masses increases with the distance of SZ and X-ray offsets. However, in *Sample 2* it is noticeable that these correlations occur in slightly different scalings. In 4.4 (ii), TMD offsets in the range of 0.2 to 0.3 R/r_{500c} only occur at the largest offsets in SZ and X-ray, whereas in (i), high TMD offsets in the same range can already be detected at lower SZ and X-ray offsets. It should also be noted that the scatter in (i) is almost evenly distributed over the offset ranges. However in (ii), an accumulation at small SZ and X-ray offsets exhibits. Separated by a diffuse gap of data points, only a reduced distribution at larger offsets catches the eye. The difference in the offset distributions could be the result of low initial velocities of subclusters, as also suggested by (Zhang et al., 2014) - in fact, a difference between *Sample 1* and *Sample 2* can definitely be noticed, especially in the x -range of 0.25 to 0.4 R/r_{500c} . In this interval, a region (gray area) was placed in order to constitute the amount of included clusters. By comparing Subfigure 4.4 (i) and (ii), only 6 clusters hosting no shocks were detected in this range, whereas up to 17 clusters hosting shocks have been counted occurring under these specific offset ranges. By considering these results, the probability that detected galaxy clusters in the range of 0.25 to 0.4 R/r_{500c} could host shocks is 73.91%, so the correlations partially indicate whether a shock can be detected or not. In fact, the chance of detecting shocks is slightly increased by considering only strong offsets. An absolute certainty, however, can not be provided, since Subfigure 4.4 (ii) also shows that, even if there are strong offsets in different categories detected, shocks cannot necessarily be detected.

The fact that SZ and X-ray peak offsets are oriented towards the same direction, as showcased in Figure 3.4, proved to be the exception rather than the rule would lead to randomly distributed offset relations. These counter examples, however, were only taken from considering the brightest peaks, but not their brightness centroids. In order to obtain this linear scaling relation, the centroid peaks must indeed point towards the same directions relative to the target's barycenter.

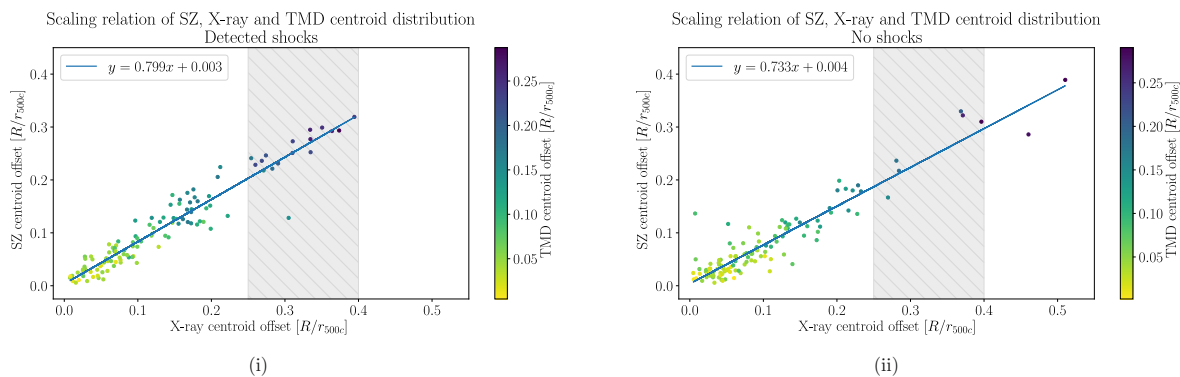


Figure 4.4: Scatter plots of X-ray and SZ offsets. The TMD offset distribution is color-coded from yellow to violet for increasing distances. The data was extracted from *Sample 1* and *Sample 2*.

In both samples, the slope is less than one, which suggests that a certain X-ray displacement is always slightly larger than an SZ offset (e.g., in Subfigure 4.4 (i), the SZ centroid offset is behind the X-ray centroid by a factor of 0.799). Assuming both centroids would point in approximately the same direction, one could conclude that the X-ray peak is statistically pointing stronger towards the clusters peripheries, hence tracing a possible shock. On the

other hand, Subfigure 4.4 (ii) also has a slope less than one, which means that the SZ centroid would still be located behind an X-ray centroid, independently of occurrences of shocks. However, the exact slope of (ii) should not be taken into account, since the scattering tends to increase for higher SZ and X-ray offsets.

Assuming both centroids are located on the same axis pointing in the same direction would suggest an increase in the SZ-X-ray offset during the merger process. However, SZ-X-ray displacements within this offset range of less than the half of r_{500c} are negligibly small and already resulted in random fluctuations in the range of 0 to $0.14 R/r_{500c}$ (as shown in Figure 4.3). By considering the slopes in Figure 4.4, the strong and random scatter effects could only decrease at larger scales (around multiple r_{500c}), which would render a prediction for SZ-X-ray offset distances coming from a given SZ or X-ray offset unrealistic. This effect only occurs due to the calculated brightness centroids - that being said, it is justifiable to conclude that a large SZ centroid shift will presumably imply an X-ray centroid to be offset at a similar distance and vice versa. Taking the linear distribution of the TMD relative to the SZ and X-ray peaks into account, this conclusion would still hold by measuring mass distribution centroid offsets.

Chapter 5

Discussion

5.1 Conclusion

To sum up the results of this work, it should be noted that the evaluation and categorization of shocks and their physical properties succumbs (at least to a certain degree) the subjective perception of the author - for instance, detecting overpressured areas at the peripheries of the cluster as shocks could not always be done unambiguously. However, from a statistical perspective, the initial dataset consisting of 1043 galaxy clusters should have been large enough to outweigh small variations of wrongly categorized clusters. Aside from subjective interpretations of the measurement data, projection effects (as shown in Figure 3.5) account for another source of uncertainty. In consideration of statistical variations, the main results are briefly discussed in the following Subsections.

5.1.1 Assignment of Selective Surface Brightness Peaks and Centroid Offsets

In Section 3.2, it was shown that offset selective surface brightness peaks, e.g., the SZ effect, do not strictly relate to corresponding shocks. According to Kale et al. (2017), a galaxy cluster with the SZ peak is oriented towards the radio relic, and the X-ray peak oriented towards its center, has been reported. However, a considerable proportion of the opposite constellation was found to amount up to 8.55%. This instability of constellation could occur due to very bright subclusters not necessarily belonging to the merger. In order to still obtain a sufficient evidence considering brightness peak orientations, the SZ and X-ray centroid peaks were calculated for further analysis. This led to the following correlations:

- ① Due to the two-dimensional projection from a three-dimensional merger, it is possible in some cases to detect shocks propagating from an equatorial origin. Since the collision axis could be perpendicular to the projection plane, no SZ and X-ray peaks can be observed, which means that a detected SZ-X-ray offset could imply that a shock was found. A possible SZ and X-ray peak offset, however, cannot be inferred from a found shock, since equatorial shocks (which could be misinterpreted as axial shocks) can be detected as well.
- ② The largest SZ-X-ray peak offset, which amounts to 304.09 kpc, was found in galaxy cluster 461. This is less than a half of the reported offset in cluster PLCK G200.9-28.2.
- ③ The SZ-X-ray centroid offsets are a lot smaller than SZ-X-ray peak offsets and do not differ over such a large range as the peak offsets.

- ④ When measuring the SZ and X-ray centroid offsets relative to the barycenter of the most massive subcluster, the mean SZ centroid offset peak tends to fall behind the X-ray centroid peak, which can be revealed in *Sample 1* and *Sample 2* (see Figure 3.7). The only differences in *Sample 1* are a mean offset distribution more oriented towards the cluster's peripheries, and a wider distribution spreading in the range of 0 to $0.4 R/r_{500c}$.
- ⑤ The observed distribution shape of X-ray centroid shifts is comparable with the simulated ones. The mean centroid shifts, however, show a larger offset in the simulated data indicating a generally more dynamic state of galaxy clusters compared to the data obtained by observations (see Figure 3.8).
- ⑥ The centroid of the TMD distribution is less offset than the SZ and X-ray centroids. The offset distribution shape of the TMD is comparable to the distributions mentioned in key point ④ (also see Figure 4.2).
- ⑦ The SZ and X-ray centroid offsets are related linearly to each other, whereas the SZ offset falls behind the X-ray offset by a fitted factor of 0.799. The TMD centroid offsets also scale with the SZ and X-ray offsets. *Sample 2* leaks in clusters hosting SZ and X-ray offsets larger than $0.25 R/r_{500c}$. Hence, larger offsets can indicate a higher probability to detect merger shocks in galaxy clusters.

5.1.2 Observational Feasibility

From an observational point of view, the most interesting question is whether radio relics can be observed under the condition of high offsets in measurable cluster's properties or not. Comparing *Sample 1* and *Sample 2*, a greater difference in terms of the centroid offsets of SZ and X-ray emissions (see Figure 4.4 (i)) can be seen in higher ranges, i.e., $0.25 R/r_{500c}$ or above. In this range, clusters occurred more frequently in *Sample 1* than in *Sample 2*, hence hosting shocks. In consideration of these datasets, the chance of finding shocks in this certain range amounts to 73.01%. By comparing both samples in the range of less than $0.25 R/r_{500c}$ of SZ or X-ray centroid offsets, no significant statement can be proposed anymore. Regarding observational data, it could be promising to find shocked gas and therefore radio relics, once a mean SZ or X-ray centroid offset of more than $0.25 R/r_{500c}$ relative to the target's barycenter is exceeded. Since the barycenter of the subcluster can only be identified by gravitational lensing effects, this method provides additional observational data. In a recent study, where a team of researches reported observational confirmation of new strong gravitational lensing systems, one can get an idea of how many iterative steps are required in order to obtain justifiable results (Nord et al., 2020). On the other hand, a large observational X-ray centroid shift dataset provided by Yuan and Han (2020) was obtained using Equation 3.2. Since the distribution shapes of the X-ray centroid shifts, as shown in Figure 3.8 only differ in a higher mean centroid shift in the simulated data due to the initially set constraint of only considering merging subclusters, it could be promising to study the observed galaxy clusters hosting high centroid shifts in order to increase the chance of detecting radio relics.

5.2 Outlook

Since *Sample 1* amounts to 117 merging galaxy clusters, the vast dataset consisting of 964 observed galaxy clusters with its centroid shifts ω (calculated by Yuan and Han (2020)) would be an interesting source to compare larger datasets of simulated X-ray centroid shifts.

Furthermore, due to the two-dimensional projection, it could have been possible that equatorial shocks have been detected and could have been mistakenly assigned to axial merger shocks. Consequently, a parallel merger projection was considered, but since the merger axis is perpendicular to the projection plane no SZ and X-ray peak offsets could have been detected. For future investigations, it could be promising to consider the three-dimensional cluster constellations, which can be extracted via the tool SIMCUT from the Web Portal.

In the future, the scaling relation of the SZ-X-ray-TMD centroid shifts (see Figure 4.4) could be studied in greater detail, leading to a better understanding of the interaction of Baryonic and Dark Matter in galaxy clusters.

Bibliography

- W. Burger and M. J. Burge. *Digital Image Processing*. Springer London, 2016. doi: 10.1007/978-1-4471-6684-9.
- J. E. Carlstrom, G. P. Holder, and E. D. Reese. Cosmology with the Sunyaev-Zel'dovich Effect. *Annual Review of Astronomy and Astrophysics*, 40(1):643–680, sep 2002. doi: 10.1146/annurev.astro.40.060401.093803.
- B. Carroll. *An introduction to modern astrophysics*. Pearson, City, 2014. ISBN 9781292022932.
- M. H. Chan. A universal constant for dark matter-baryon interplay. *Scientific Reports*, 9(1):1, mar 2019. doi: 10.1038/s41598-019-39717-x.
- K. Dolag, F. K. Hansen, M. Roncarelli, and L. Moscardini. The imprints of local superclusters on the Sunyaev-Zel'dovich signals and their detectability with Planck. *Monthly Notices of the Royal Astronomical Society*, 363(1):29–39, oct 2005. doi: 10.1111/j.1365-2966.2005.09452.x.
- K. Dolag, S. Borgani, G. Murante, and V. Springel. Substructures in hydrodynamical cluster simulations. *Monthly Notices of the Royal Astronomical Society*, 399(2):497–514, oct 2009. doi: 10.1111/j.1365-2966.2009.15034.x.
- A. E. Evrard, J. J. Mohr, D. G. Fabricant, and M. J. Geller. A Morphology-Cosmology Connection for X-Ray Clusters. *apjl*, 419:L9, Dec. 1993. doi: 10.1086/187124. URL <https://ui.adsabs.harvard.edu/abs/1993ApJ...419L...9E>.
- J.-H. Ha, D. Ryu, and H. Kang. Properties of Merger Shocks in Merging Galaxy Clusters. *The Astrophysical Journal*, 857(1):1, apr 2018. doi: 10.3847/1538-4357/aab4a2.
- R. Kale, D. R. Wik, S. Giacintucci, T. Venturi, G. Brunetti, R. Cassano, D. Dallacasa, and F. de Gasperin. Discovery of a radio relic in the low mass, merging galaxy cluster PLCK G200.9-28.2. *Monthly Notices of the Royal Astronomical Society*, 472(1):940–948, aug 2017. doi: 10.1093/mnras/stx2031.
- H. Kolanoski and N. Wermes. *Teilchendetektoren*. Springer Berlin Heidelberg, 2016. doi: 10.1007/978-3-662-45350-6.
- K. Konar, K. Bose, and R. K. Paul. Revisiting cosmic microwave background radiation using blackbody radiation inversion. *Scientific Reports*, 11(1), jan 2021. doi: 10.1038/s41598-020-80195-3.
- M. S. Longair. *High Energy Astrophysics*. CAMBRIDGE, Feb. 2011. ISBN 0521756189. URL https://www.ebook.de/de/product/11904559/malcolm_s_longair_high_energy_astrophysics.html.
- C. Mastropietro and A. Burkert. Simulating the Bullet Cluster. *Monthly Notices of the Royal Astronomical Society*, 389(2):967–988, sep 2008. doi: 10.1111/j.1365-2966.2008.13626.x.

- B. J. Maughan, C. Jones, W. Forman, and L. Van Speybroeck. Images, Structural Properties, and Metal Abundances of Galaxy Clusters Observed with Chandra ACIS-I at $0.1 < z < 1.3$. *apjs*, 174(1):117–135, Jan. 2008. doi: 10.1086/521225. URL <https://ui.adsabs.harvard.edu/abs/2008ApJS...174..117M>.
- V. Mukhanov. *Physical foundations of cosmology*. Cambridge University Press, Cambridge, UK New York, 2005. ISBN 9780511136795.
- B. Nord, E. Buckley-Geer, H. Lin, N. Kuropatkin, T. Collett, D. L. Tucker, H. T. Diehl, A. Agnello, A. Amara, T. M. C. Abbott, S. Allam, J. Annis, S. Avila, K. Bechtol, D. Brooks, D. L. Burke, A. C. Rosell, M. C. Kind, J. Carretero, C. E. Cunha, L. N. da Costa, C. Davis, J. D. Vicente, P. Doel, T. F. Eifler, A. E. Evrard, E. Fernandez, B. Flaugher, P. Fosalba, J. Frieman, J. García-Bellido, E. Gaztanaga, D. Gruen, R. A. Gruendl, G. Gutierrez, W. G. Hartley, D. L. Hollowood, K. Honscheid, B. Hoyle, D. J. James, K. Kuehn, O. Lahav, M. Lima, M. A. G. Maia, M. March, J. L. Marshall, P. Melchior, F. Menanteau, R. Miquel, A. A. Plazas, A. K. Romer, A. Roodman, E. S. Rykoff, E. Sanchez, V. Scarpine, R. Schindler, M. Schubnell, I. Sevilla-Noarbe, M. Smith, M. Soares-Santos, F. Sobreira, E. Suchyta, M. E. C. Swanson, G. Tarle, D. Thomas, and Y. Z. and. Observation and confirmation of nine strong-lensing systems in Dark Energy Survey Year 1 data. *Monthly Notices of the Royal Astronomical Society*, 494(1):1308–1322, jan 2020. doi: 10.1093/mnras/staa200.
- S. Planelles, D. Fabjan, S. Borgani, G. Murante, E. Rasia, V. Biffi, N. Truong, C. Ragone-Figueroa, G. L. Granato, K. Dolag, E. Pierpaoli, A. M. Beck, L. K. Steinborn, and M. Gaspari. Pressure of the hot gas in simulations of galaxy clusters. *Monthly Notices of the Royal Astronomical Society*, 467(4):2, feb 2017. doi: 10.1093/mnras/stx318.
- G. B. Poole, M. A. Fardal, A. Babul, I. G. McCarthy, T. Quinn, and J. Wadsley. The impact of mergers on relaxed X-ray clusters – I. Dynamical evolution and emergent transient structures. *Monthly Notices of the Royal Astronomical Society*, 373(3):881–905, nov 2006. doi: 10.1111/j.1365-2966.2006.10916.x.
- A. Ragagnin, K. Dolag, V. Biffi, M. C. Bel, N. J. Hammer, A. Krukau, M. Petkova, and D. Steinborn. A web portal for hydrodynamical, cosmological simulations. page 3, Dec. 2016.
- P. Schneider. *Einführung in die Extragalaktische Astronomie und Kosmologie*. Springer-Verlag GmbH, Feb. 2006. ISBN 9783540305897. URL https://www.ebook.de/de/product/19205509/peter_schneider_einfuehrung_in_die_extragalaktische_astronomie_und_kosmologie.html.
- R. A. Sunyaev and Y. B. Zeldovich. Small-Scale Fluctuations of Relic Radiation. *apss*, 7(1):3–19, Apr. 1970. doi: 10.1007/BF00653471. URL <https://ui.adsabs.harvard.edu/abs/1970Ap&SS...7....3S>.
- R. J. van Weeren, F. de Gasperin, H. Akamatsu, M. Brüggen, L. Feretti, H. Kang, A. Stroe, and F. Zandanel. Diffuse Radio Emission from Galaxy Clusters. *Space Science Reviews*, 215(1):8, feb 2019. doi: 10.1007/s11214-019-0584-z.
- S. M. S. A. O. William Joye (Smithsonian Astrophysical Observatory), Eric Mandel (Smithsonian Astrophysical Observatory). SAO Image DS9. <https://sites.google.com/cfa.harvard.edu/saoimageds9/home>, 2021.
- Z. S. Yuan and J. L. Han. Dynamical state for 964 galaxy clusters from Chandra X-ray images. *Monthly Notices of the Royal Astronomical Society*, 497(4):5485–5497, aug 2020. doi: 10.1093/mnras/staa2363.

-
- C. Zhang, Q. Yu, and Y. Lu. OFFSETS BETWEEN THE x-RAY AND THE SUNYAEV-ZEL'DOVICH-EFFECT PEAKS IN MERGING GALAXY CLUSTERS AND THEIR COSMOLOGICAL IMPLICATIONS. *The Astrophysical Journal*, 796(2):1, nov 2014. doi: 10.1088/0004-637x/796/2/138.

List of Figures

1.1	An illustration of an ideal head-on collision of two infalling substructures. . .	1
1.2	Example of a merging galaxy cluster accomodating an offset X-ray peak relative to its potential minimum. This cluster hosts shocks and was extracted from the tool SMAC of the cosmological simulation Magneticum.	2
1.3	Scattered CMBR by electrons in the ICM.	3
1.4	A geometric scetch of the inverse compton scattering.	3
1.5	Sketch of a shockwave propagating along the distance d . In the limit, the shock originates from a discontinuous jump between the two different states x_1 and x_2 over a small limiting process δ	5
1.6	Pertubation of particles after crossing the shock region. The shock wave propagates in upstream direction.	5
1.7	Idealized morphology of a head-on merging galaxy cluster. The most energetic and most offset shock from the baryonic matter is in front of the light DM clump along the merger axis.	6
2.1	Illustration of a FITS file. Every pixel hosts a certain physical value and can be identified by its coordinate.	11
2.2	Calculating distances in bitmaps.	11
2.3	Measuring the distance of a shock propagating through space over time with DS9.	12
2.4	Radial binning of a FITS file. The dashed lines mark the boundaries of every bin. Hence, in total there are four bins. In every bin there are different pixel values distributed in a certain range.	13
2.5	Gaussian filtering process of cluster number 65 at redshift $z = 0.29$. The Compton- y parameter is color-coded from blue to yellow for increasing values.	14
3.1	Example clusters for assigned categories.	16
3.2	Comparison of (i) the reported cluster (PLCK G200.9-28.2) by Kale et al. (2017), observed by the Giant Metrowave Radio Telescope (GMRT) in the 610 MHz spectrum, to (ii) the simulated cluster (Cluster ID 479). Both host a shock in the cluster's periphery. In (i) and (ii), the SZ and X-ray peaks are marked as + and \times , respectively. However, the SZ-X-ray offset, as marked in (ii), is a lot smaller than in (i).	16
3.3	Radial profiles of Cluster 479.	17

3.4	Centered SZ signal peak and offset X-ray peak.	18
3.5	Three kinds of appearances of different projection scenarios, which occur when a three-dimensional collision is mapped onto a two-dimensional plane. Here, (i) is a perpendicular projection, (ii) is a slightly shifted projection and (iii) is a parallel projection relative to the collision axis. The blue and red spheres can either represent SZ or X-ray peaks, as already discussed previously.	18
3.6	Histogram of the distribution of SZ-X-ray displacements in units of the physical radius, normalized by r_{500c} . The clusters with detected shocks are labelled in light blue, whereas clusters hosting no detected shocks are colored in orange. The histogram in (i) was taken by considering only the surface brightness peaks. (ii) displays the same samples, however taken the emission centroids from the SZ and X-ray surface brightnesses.	19
3.7	Histograms of the SZ and X-ray centroid offset distributions. In (i), the distribution was extracted from the dataset, where shocks have been detected, whereas in (ii), the dataset hosting no shocks was taken into account.	20
3.8	Comparison of the by Magneticum simulated and the observed centroid shift ω provided by Yuan and Han (2020). In Subfigure (i) <i>Sample 1</i> was compared to the observations, whereas <i>Sample 2</i> was investigated in Subfigure (ii).	21
4.1	Ongoing merger at four different states from $z = 0.38$ to $z = 0.25$. The direction of the shock and morphology can be extracted from the relative pressure frames, whereas the Compton- y and the X-ray maps illustrate offset brightness peaks and the total mass density mainly traces the DM clumps.	24
4.2	TMD centroid offset distribution of <i>Sample 1</i> (i) and <i>Sample 2</i> (ii). The mean offset in (ii) shows a slight decrease, amounting to approximately 2.6% in distance in comparison to (i).	25
4.3	Scatter plot of (i), the SZ centroid shift and SZ-X-ray displacement, and (ii), the X-ray centroid shift and SZ-X-ray displacement. In the small SZ-X-ray range of 0 to $0.14 R/r_{500c}$, both plots show strong displacement fluctuations.	25
4.4	Scatter plots of X-ray and SZ offsets. The TMD offset distribution is color-coded from yellow to violet for increasing distances. The data was extracted from <i>Sample 1</i> and <i>Sample 2</i>	26

List of Tables

2.1	Parameters of <i>Box2b/hr</i> , extracted from the cosmological web portal.	9
2.2	Constraints for the dataset, which have been used for further analysis.	10
3.1	Morphological distribution of detected shocks from the dataset consisting of 1043 merging clusters.	15
3.2	Distribution of SZ-X-ray offset combinations. In this Table A, B, C and D are labelled as <i>SZ peak in shock direction</i> , <i>X-ray peak in shock direction</i> , <i>SZ & X-ray peak in shock direction</i> and <i>No correlation</i> , respectively.	17
A.1	Table 1 of galaxy clusters where shocks have been detected.	43
A.2	Table 2 of galaxy clusters where shocks have been detected.	44
A.3	Table 3 of galaxy clusters where shocks have been detected.	45
A.4	Table 4 of galaxy clusters where shocks have been detected.	46

Appendices

Appendix A

Data Tables

A.1 List of Merging Clusters with Detected Shocks

For the following tables of galaxy clusters where shocks have been detected, arranged by r_{500c} , the columns are labelled as follows:

- A: SZ peak offset
- B: X-ray peak offset
- C: SZ centroid shift
- D: X-ray centroid shift
- E: SZ-X-ray peak displacement
- F: SZ-X-ray centroid displacement
- G: r_{500c}

A	B	C	D	E	F	G
$4.22 \cdot 10^{-2}$	$1.25 \cdot 10^{-2}$	$4.32 \cdot 10^{-2}$	$9.86 \cdot 10^{-2}$	$3.35 \cdot 10^{-2}$	$3.64 \cdot 10^{-2}$	648.3
$2.21 \cdot 10^{-2}$	$6.79 \cdot 10^{-3}$	$7.35 \cdot 10^{-2}$	0.13	$1.76 \cdot 10^{-2}$	$3.58 \cdot 10^{-2}$	648.34
$4.86 \cdot 10^{-2}$	$2.04 \cdot 10^{-2}$	$2.23 \cdot 10^{-2}$	$2.45 \cdot 10^{-2}$	$2.74 \cdot 10^{-2}$	$8.86 \cdot 10^{-3}$	648.43
0.11	$2.86 \cdot 10^{-2}$	0.12	0.13	$5.05 \cdot 10^{-2}$	$1.93 \cdot 10^{-2}$	649.78
$6.79 \cdot 10^{-3}$	$3.99 \cdot 10^{-2}$	0.22	0.27	$2.77 \cdot 10^{-2}$	$3.59 \cdot 10^{-2}$	652.25
0.16	0.24	$5.43 \cdot 10^{-2}$	$9.26 \cdot 10^{-2}$	$5.15 \cdot 10^{-2}$	$3.55 \cdot 10^{-2}$	653.38
$5.8 \cdot 10^{-2}$	$6.14 \cdot 10^{-2}$	$8.82 \cdot 10^{-3}$	$3.11 \cdot 10^{-2}$	$2.8 \cdot 10^{-3}$	$1.69 \cdot 10^{-2}$	653.54
$6.14 \cdot 10^{-2}$	$8.63 \cdot 10^{-2}$	$2.81 \cdot 10^{-2}$	$5.87 \cdot 10^{-2}$	$1.64 \cdot 10^{-2}$	$2.07 \cdot 10^{-2}$	654.39
0.14	$1.52 \cdot 10^{-2}$	$5.36 \cdot 10^{-2}$	$8.78 \cdot 10^{-2}$	$8.39 \cdot 10^{-2}$	$3.04 \cdot 10^{-2}$	655.59
$1.25 \cdot 10^{-2}$	$1.09 \cdot 10^{-2}$	$5.8 \cdot 10^{-2}$	$8.54 \cdot 10^{-2}$	$8.9 \cdot 10^{-3}$	$1.96 \cdot 10^{-2}$	655.62
$3.23 \cdot 10^{-2}$	$1.85 \cdot 10^{-2}$	0.13	0.15	$1.41 \cdot 10^{-2}$	$1.35 \cdot 10^{-2}$	655.67
$3.75 \cdot 10^{-2}$	0.1	$3.61 \cdot 10^{-2}$	$2.75 \cdot 10^{-2}$	$4.3 \cdot 10^{-2}$	$6.03 \cdot 10^{-3}$	657.65
$4.59 \cdot 10^{-2}$	$9.1 \cdot 10^{-3}$	0.21	0.21	$3.01 \cdot 10^{-2}$	$2.37 \cdot 10^{-3}$	658.82
$2.45 \cdot 10^{-2}$	$1.63 \cdot 10^{-2}$	$8.86 \cdot 10^{-3}$	$1.15 \cdot 10^{-2}$	$2.08 \cdot 10^{-2}$	$9.39 \cdot 10^{-3}$	666.1

Table A.1: Table 1 of galaxy clusters where shocks have been detected.

A	B	C	D	E	F	G
$8.35 \cdot 10^{-2}$	$5.3 \cdot 10^{-2}$	0.14	0.17	$2.07 \cdot 10^{-2}$	$2.47 \cdot 10^{-2}$	668.91
0.14	$2.86 \cdot 10^{-2}$	0.24	0.27	$8.62 \cdot 10^{-2}$	$2.18 \cdot 10^{-2}$	669.31
0.61	0.6	0.29	0.36	$1.55 \cdot 10^{-2}$	$5.52 \cdot 10^{-2}$	669.48
$1.85 \cdot 10^{-2}$	$3.03 \cdot 10^{-3}$	0.12	$9.65 \cdot 10^{-2}$	$1.04 \cdot 10^{-2}$	$2.93 \cdot 10^{-2}$	670.62
$2.21 \cdot 10^{-2}$	$3.75 \cdot 10^{-2}$	$4.87 \cdot 10^{-2}$	$7.64 \cdot 10^{-2}$	$1.04 \cdot 10^{-2}$	$2.05 \cdot 10^{-2}$	670.94
0.22	0.19	0.12	0.16	$2.46 \cdot 10^{-2}$	$2.58 \cdot 10^{-2}$	671.52
$2.21 \cdot 10^{-2}$	$2.86 \cdot 10^{-2}$	$6.58 \cdot 10^{-2}$	$6.83 \cdot 10^{-2}$	$3.38 \cdot 10^{-2}$	$1.02 \cdot 10^{-2}$	673.09
0.2	$3.39 \cdot 10^{-2}$	0.25	0.31	0.16	$4.02 \cdot 10^{-2}$	676.68
$3.39 \cdot 10^{-2}$	$5.3 \cdot 10^{-2}$	0.18	0.18	$1.46 \cdot 10^{-2}$	$4.44 \cdot 10^{-3}$	678.57
$2.8 \cdot 10^{-2}$	$3.03 \cdot 10^{-3}$	0.11	0.2	$2.1 \cdot 10^{-2}$	$6.37 \cdot 10^{-2}$	679.98
$2.59 \cdot 10^{-2}$	$2.45 \cdot 10^{-2}$	$3.71 \cdot 10^{-2}$	$4.88 \cdot 10^{-2}$	$1.17 \cdot 10^{-2}$	$1.83 \cdot 10^{-2}$	680.46
$8.76 \cdot 10^{-2}$	$4.13 \cdot 10^{-2}$	0.32	0.39	$4.21 \cdot 10^{-2}$	$5.17 \cdot 10^{-2}$	680.76
$5.47 \cdot 10^{-2}$	$2.99 \cdot 10^{-2}$	0.12	0.19	$2.14 \cdot 10^{-2}$	$4.7 \cdot 10^{-2}$	685.95
$1.85 \cdot 10^{-2}$	$2.99 \cdot 10^{-2}$	$9.35 \cdot 10^{-2}$	$9.69 \cdot 10^{-2}$	$1.72 \cdot 10^{-2}$	$1.71 \cdot 10^{-2}$	689.11
$5.77 \cdot 10^{-2}$	$1.09 \cdot 10^{-2}$	$1.46 \cdot 10^{-2}$	$4.66 \cdot 10^{-2}$	$3.39 \cdot 10^{-2}$	$3.15 \cdot 10^{-2}$	693.06
$1.63 \cdot 10^{-2}$	$1.52 \cdot 10^{-2}$	$5 \cdot 10^{-2}$	$5.92 \cdot 10^{-2}$	$2.98 \cdot 10^{-3}$	$1.66 \cdot 10^{-2}$	694.89
$1.63 \cdot 10^{-2}$	$1.94 \cdot 10^{-2}$	$2.49 \cdot 10^{-2}$	$1.82 \cdot 10^{-2}$	$2.42 \cdot 10^{-2}$	$1.19 \cdot 10^{-2}$	698.12
$9.94 \cdot 10^{-2}$	0.19	0.11	0.12	$6.6 \cdot 10^{-2}$	$1.63 \cdot 10^{-2}$	698.23
$1.09 \cdot 10^{-2}$	$2.37 \cdot 10^{-2}$	$5.53 \cdot 10^{-2}$	$3.64 \cdot 10^{-2}$	$1.76 \cdot 10^{-2}$	$1.79 \cdot 10^{-2}$	701.98
$4.71 \cdot 10^{-2}$	$2.04 \cdot 10^{-2}$	0.24	0.25	$1.94 \cdot 10^{-2}$	$9.38 \cdot 10^{-3}$	705.08
0.33	0.54	0.3	0.35	0.15	$3.67 \cdot 10^{-2}$	706.66
$3.05 \cdot 10^{-2}$	0.63	0.13	0.16	0.43	$2.68 \cdot 10^{-2}$	710.26
$4.51 \cdot 10^{-2}$	$2.37 \cdot 10^{-2}$	0.12	0.18	$1.56 \cdot 10^{-2}$	$4.65 \cdot 10^{-2}$	713.35
0.2	0.36	0.28	0.33	0.16	$4.3 \cdot 10^{-2}$	714.67
$7.08 \cdot 10^{-2}$	0.62	0.13	0.22	0.42	$6.44 \cdot 10^{-2}$	714.8
$6.79 \cdot 10^{-3}$	$2.86 \cdot 10^{-2}$	$2.62 \cdot 10^{-2}$	$3.58 \cdot 10^{-2}$	$2.54 \cdot 10^{-2}$	$6.92 \cdot 10^{-3}$	716.51
0.51	0.63	0.29	0.33	0.1	$2.96 \cdot 10^{-2}$	719.65
0.13	0.14	0.16	0.17	$2.42 \cdot 10^{-2}$	$1.04 \cdot 10^{-2}$	720.55
$3.94 \cdot 10^{-2}$	$1.85 \cdot 10^{-2}$	0.13	0.12	$1.58 \cdot 10^{-2}$	$7.58 \cdot 10^{-3}$	721.64
$4.26 \cdot 10^{-2}$	$1.85 \cdot 10^{-2}$	0.12	0.18	$1.76 \cdot 10^{-2}$	$4.72 \cdot 10^{-2}$	725.16
$3.03 \cdot 10^{-3}$	$6.79 \cdot 10^{-3}$	0.12	0.12	$3.11 \cdot 10^{-3}$	$9.98 \cdot 10^{-3}$	725.66
$6.74 \cdot 10^{-2}$	$3.34 \cdot 10^{-2}$	$8.38 \cdot 10^{-2}$	$7.34 \cdot 10^{-2}$	$2.51 \cdot 10^{-2}$	$9.69 \cdot 10^{-3}$	726.9
$8.92 \cdot 10^{-2}$	$6.26 \cdot 10^{-2}$	0.23	0.26	$2.44 \cdot 10^{-2}$	$2.5 \cdot 10^{-2}$	728.05
$1.63 \cdot 10^{-2}$	$3.03 \cdot 10^{-3}$	$8.37 \cdot 10^{-2}$	0.1	$9.9 \cdot 10^{-3}$	$2.63 \cdot 10^{-2}$	729.76

Table A.2: Table 2 of galaxy clusters where shocks have been detected.

A	B	C	D	E	F	G
0.28	0.12	0.13	0.31	0.13	0.13	730.4
$2.59 \cdot 10^{-2}$	$1.52 \cdot 10^{-2}$	$3.03 \cdot 10^{-2}$	$4.48 \cdot 10^{-2}$	$1.83 \cdot 10^{-2}$	$1.56 \cdot 10^{-2}$	732.83
$4.26 \cdot 10^{-2}$	$2.21 \cdot 10^{-2}$	$4.4 \cdot 10^{-2}$	$5.39 \cdot 10^{-2}$	$1.7 \cdot 10^{-2}$	$8.95 \cdot 10^{-3}$	734.83
$9.35 \cdot 10^{-2}$	$9.48 \cdot 10^{-2}$	$7.82 \cdot 10^{-2}$	$6.08 \cdot 10^{-2}$	$7.9 \cdot 10^{-2}$	$2.93 \cdot 10^{-2}$	736.04
0.45	$2.99 \cdot 10^{-2}$	0.25	0.33	0.31	$6.08 \cdot 10^{-2}$	736.36
$3.39 \cdot 10^{-2}$	$2.37 \cdot 10^{-2}$	$5.1 \cdot 10^{-2}$	$2.85 \cdot 10^{-2}$	$8.95 \cdot 10^{-3}$	$1.94 \cdot 10^{-2}$	737.76
$1.25 \cdot 10^{-2}$	$9.1 \cdot 10^{-3}$	$7.63 \cdot 10^{-2}$	$7.05 \cdot 10^{-2}$	$1.27 \cdot 10^{-2}$	$6.14 \cdot 10^{-3}$	739.3
$2.45 \cdot 10^{-2}$	$1.09 \cdot 10^{-2}$	$4.99 \cdot 10^{-2}$	$3.83 \cdot 10^{-2}$	$1.15 \cdot 10^{-2}$	$9.26 \cdot 10^{-3}$	740
0.25	$1.63 \cdot 10^{-2}$	0.12	0.17	0.17	$3.73 \cdot 10^{-2}$	743.33
$1.63 \cdot 10^{-2}$	$2.21 \cdot 10^{-2}$	0.13	0.13	$2.59 \cdot 10^{-2}$	$1.17 \cdot 10^{-2}$	748.07
$9.72 \cdot 10^{-2}$	$9.1 \cdot 10^{-3}$	$1.49 \cdot 10^{-2}$	$7.88 \cdot 10^{-3}$	$7.76 \cdot 10^{-2}$	$6.25 \cdot 10^{-3}$	752.77
0.22	$9.41 \cdot 10^{-2}$	$7.38 \cdot 10^{-2}$	$9.93 \cdot 10^{-2}$	$9.62 \cdot 10^{-2}$	$3.09 \cdot 10^{-2}$	753.61
$5.19 \cdot 10^{-2}$	$1.25 \cdot 10^{-2}$	0.16	0.16	$2.98 \cdot 10^{-2}$	$7.75 \cdot 10^{-3}$	753.63
$4.98 \cdot 10^{-2}$	$1.85 \cdot 10^{-2}$	$2.55 \cdot 10^{-2}$	$5.18 \cdot 10^{-2}$	$3.33 \cdot 10^{-2}$	$2.81 \cdot 10^{-2}$	754.49
$9.31 \cdot 10^{-2}$	$1.85 \cdot 10^{-2}$	$6.02 \cdot 10^{-2}$	$7.06 \cdot 10^{-2}$	$5.84 \cdot 10^{-2}$	$2.41 \cdot 10^{-2}$	754.56
$3.39 \cdot 10^{-2}$	$2.86 \cdot 10^{-2}$	$3.74 \cdot 10^{-2}$	$6.74 \cdot 10^{-2}$	$1.76 \cdot 10^{-2}$	$2.31 \cdot 10^{-2}$	761.21
$1.25 \cdot 10^{-2}$	$3.03 \cdot 10^{-3}$	$1.87 \cdot 10^{-2}$	$1.07 \cdot 10^{-2}$	$1.04 \cdot 10^{-2}$	$6.84 \cdot 10^{-3}$	766.55
$2.99 \cdot 10^{-2}$	$3.03 \cdot 10^{-3}$	$7.47 \cdot 10^{-2}$	$9.32 \cdot 10^{-2}$	$2.4 \cdot 10^{-2}$	$2.46 \cdot 10^{-2}$	768.01
$1.09 \cdot 10^{-2}$	$1.25 \cdot 10^{-2}$	0.29	0.37	$6.61 \cdot 10^{-3}$	$6.26 \cdot 10^{-2}$	769.89
$6.11 \cdot 10^{-2}$	$9.11 \cdot 10^{-2}$	$4.49 \cdot 10^{-2}$	$6.98 \cdot 10^{-2}$	$2.35 \cdot 10^{-2}$	$2.12 \cdot 10^{-2}$	775.42
$7.29 \cdot 10^{-2}$	$1.63 \cdot 10^{-2}$	0.14	0.17	$6.33 \cdot 10^{-2}$	$1.91 \cdot 10^{-2}$	782.27
$2.8 \cdot 10^{-2}$	$3.8 \cdot 10^{-2}$	$1.82 \cdot 10^{-2}$	$2.58 \cdot 10^{-2}$	$1.22 \cdot 10^{-2}$	$7.63 \cdot 10^{-3}$	788.28
$1.09 \cdot 10^{-2}$	$6.79 \cdot 10^{-3}$	$1.9 \cdot 10^{-2}$	$4.54 \cdot 10^{-2}$	$9.59 \cdot 10^{-3}$	$2.47 \cdot 10^{-2}$	789.77
$5.37 \cdot 10^{-2}$	$8.01 \cdot 10^{-2}$	$8.97 \cdot 10^{-2}$	$9.92 \cdot 10^{-2}$	$2.93 \cdot 10^{-2}$	$8.24 \cdot 10^{-3}$	794.95
$1.25 \cdot 10^{-2}$	$2.04 \cdot 10^{-2}$	$3.82 \cdot 10^{-2}$	$4.98 \cdot 10^{-2}$	$2.4 \cdot 10^{-2}$	$1.18 \cdot 10^{-2}$	798.58
0.29	$6.4 \cdot 10^{-2}$	0.23	0.29	0.18	$4.76 \cdot 10^{-2}$	798.78
$9.1 \cdot 10^{-3}$	$6.79 \cdot 10^{-3}$	$1.79 \cdot 10^{-2}$	$8.37 \cdot 10^{-3}$	$1.09 \cdot 10^{-2}$	$1.73 \cdot 10^{-2}$	804.72
$3.8 \cdot 10^{-2}$	$1.63 \cdot 10^{-2}$	$8.22 \cdot 10^{-2}$	$9.33 \cdot 10^{-2}$	$4.05 \cdot 10^{-2}$	$1.36 \cdot 10^{-2}$	809.46
0.27	0.3	0.27	0.31	$3.89 \cdot 10^{-2}$	$3.05 \cdot 10^{-2}$	810.09
$6.68 \cdot 10^{-2}$	$1.09 \cdot 10^{-2}$	$6.71 \cdot 10^{-2}$	$8.15 \cdot 10^{-2}$	$4.68 \cdot 10^{-2}$	$1.72 \cdot 10^{-2}$	811.13
$2.73 \cdot 10^{-2}$	$6.79 \cdot 10^{-3}$	0.15	0.14	$1.77 \cdot 10^{-2}$	$7.48 \cdot 10^{-3}$	825.4
$1.52 \cdot 10^{-2}$	$1.09 \cdot 10^{-2}$	$7.11 \cdot 10^{-2}$	$6.86 \cdot 10^{-2}$	$2.07 \cdot 10^{-2}$	$2.85 \cdot 10^{-2}$	826.69
$4.55 \cdot 10^{-2}$	$1.85 \cdot 10^{-2}$	0.15	0.19	$3.36 \cdot 10^{-2}$	$4.05 \cdot 10^{-2}$	829.73
$2.04 \cdot 10^{-2}$	$5.47 \cdot 10^{-2}$	$4.66 \cdot 10^{-2}$	$6.36 \cdot 10^{-2}$	$2.9 \cdot 10^{-2}$	$2.04 \cdot 10^{-2}$	837.01

Table A.3: Table 3 of galaxy clusters where shocks have been detected.

A	B	C	D	E	F	G
$4.9 \cdot 10^{-2}$	$6.79 \cdot 10^{-3}$	0.16	0.18	$3.57 \cdot 10^{-2}$	$1.9 \cdot 10^{-2}$	843.7
0.22	0.23	0.22	0.28	$1.09 \cdot 10^{-2}$	$5.22 \cdot 10^{-2}$	848.45
$6.63 \cdot 10^{-2}$	$9.43 \cdot 10^{-2}$	$9.82 \cdot 10^{-2}$	0.12	$2.79 \cdot 10^{-2}$	$2 \cdot 10^{-2}$	853.8
$1.63 \cdot 10^{-2}$	$2.86 \cdot 10^{-2}$	$2.86 \cdot 10^{-2}$	$2.52 \cdot 10^{-2}$	$2 \cdot 10^{-2}$	$3.64 \cdot 10^{-3}$	866.32
$1.85 \cdot 10^{-2}$	$6.79 \cdot 10^{-3}$	$3.21 \cdot 10^{-2}$	$2.81 \cdot 10^{-2}$	$1.18 \cdot 10^{-2}$	$1.07 \cdot 10^{-2}$	870.78
$6.74 \cdot 10^{-2}$	$5.8 \cdot 10^{-2}$	0.13	0.15	$1.06 \cdot 10^{-2}$	$2.94 \cdot 10^{-2}$	874.91
$4.86 \cdot 10^{-2}$	$1.25 \cdot 10^{-2}$	$5.86 \cdot 10^{-3}$	$1.57 \cdot 10^{-2}$	$4.2 \cdot 10^{-2}$	$1.86 \cdot 10^{-2}$	876.03
$4.34 \cdot 10^{-2}$	$3.94 \cdot 10^{-2}$	0.15	0.16	$4.71 \cdot 10^{-2}$	$1.42 \cdot 10^{-2}$	887.51
$3.99 \cdot 10^{-2}$	$3.75 \cdot 10^{-2}$	0.17	0.15	$3.81 \cdot 10^{-3}$	$2.19 \cdot 10^{-2}$	888.23
$4.9 \cdot 10^{-2}$	$1.52 \cdot 10^{-2}$	$1.66 \cdot 10^{-2}$	$3.92 \cdot 10^{-2}$	$3.13 \cdot 10^{-2}$	$2.27 \cdot 10^{-2}$	903.82
0.27	$2.21 \cdot 10^{-2}$	$9.47 \cdot 10^{-2}$	0.12	0.25	$2.66 \cdot 10^{-2}$	906.6
$2.8 \cdot 10^{-2}$	$4.08 \cdot 10^{-2}$	0.17	0.18	$2.23 \cdot 10^{-2}$	$2.84 \cdot 10^{-2}$	918.94
$4.26 \cdot 10^{-2}$	$1.09 \cdot 10^{-2}$	$5.33 \cdot 10^{-2}$	$7.52 \cdot 10^{-2}$	$3.54 \cdot 10^{-2}$	$2.04 \cdot 10^{-2}$	923.33
$9.15 \cdot 10^{-2}$	$3.39 \cdot 10^{-2}$	0.22	0.21	$5.54 \cdot 10^{-2}$	$1.57 \cdot 10^{-2}$	929.13
$8.19 \cdot 10^{-2}$	0.11	$6.51 \cdot 10^{-2}$	$6.97 \cdot 10^{-2}$	$6.27 \cdot 10^{-2}$	$4.42 \cdot 10^{-3}$	935.37
0.3	0.4	0.15	0.2	0.1	$4.59 \cdot 10^{-2}$	939.45
$3.94 \cdot 10^{-2}$	$5.8 \cdot 10^{-2}$	$5.96 \cdot 10^{-2}$	$8.07 \cdot 10^{-2}$	$2.85 \cdot 10^{-2}$	$2.07 \cdot 10^{-2}$	947.32
$6.82 \cdot 10^{-2}$	$4.94 \cdot 10^{-2}$	$3.07 \cdot 10^{-2}$	$2.54 \cdot 10^{-2}$	$2.05 \cdot 10^{-2}$	$1.75 \cdot 10^{-2}$	953.87
$5.3 \cdot 10^{-2}$	$3.65 \cdot 10^{-2}$	$5.19 \cdot 10^{-2}$	$5.71 \cdot 10^{-2}$	$2.13 \cdot 10^{-2}$	$2.34 \cdot 10^{-2}$	972.28
0.23	$7.11 \cdot 10^{-2}$	$9.15 \cdot 10^{-2}$	0.14	0.2	$6.16 \cdot 10^{-2}$	1,001.39
$9.88 \cdot 10^{-2}$	0.19	$4.39 \cdot 10^{-2}$	$7.66 \cdot 10^{-2}$	$9.62 \cdot 10^{-2}$	$3.3 \cdot 10^{-2}$	1,009.18
$8.88 \cdot 10^{-2}$	$5.86 \cdot 10^{-2}$	$6.3 \cdot 10^{-2}$	$6.11 \cdot 10^{-2}$	$3.53 \cdot 10^{-2}$	$2.44 \cdot 10^{-2}$	1,019.01
$3.8 \cdot 10^{-2}$	$2.45 \cdot 10^{-2}$	0.12	0.17	$2.2 \cdot 10^{-2}$	$6.14 \cdot 10^{-2}$	1,024.8
$4.9 \cdot 10^{-2}$	$5.37 \cdot 10^{-2}$	0.25	0.27	$1.97 \cdot 10^{-2}$	$3.41 \cdot 10^{-2}$	1,027.29
$5.98 \cdot 10^{-2}$	$2.8 \cdot 10^{-2}$	$7.18 \cdot 10^{-2}$	$6.6 \cdot 10^{-2}$	$3.6 \cdot 10^{-2}$	$1.34 \cdot 10^{-2}$	1,047.66
$2.99 \cdot 10^{-2}$	$5.47 \cdot 10^{-2}$	0.14	0.17	$2.73 \cdot 10^{-2}$	$4.84 \cdot 10^{-2}$	1,061.92
$2.21 \cdot 10^{-2}$	$1.94 \cdot 10^{-2}$	$5.51 \cdot 10^{-2}$	$2.8 \cdot 10^{-2}$	$3.72 \cdot 10^{-2}$	$2.91 \cdot 10^{-2}$	1,075.06
$3.03 \cdot 10^{-3}$	$1.09 \cdot 10^{-2}$	$1.07 \cdot 10^{-2}$	$1.98 \cdot 10^{-2}$	$1.39 \cdot 10^{-2}$	$1.59 \cdot 10^{-2}$	1,079.75
$6.79 \cdot 10^{-3}$	$1.52 \cdot 10^{-2}$	$4.65 \cdot 10^{-2}$	$5.9 \cdot 10^{-2}$	$1.06 \cdot 10^{-2}$	$2.37 \cdot 10^{-2}$	1,107.12
0.1	$6.63 \cdot 10^{-2}$	$9.45 \cdot 10^{-2}$	0.14	$3.97 \cdot 10^{-2}$	$5.07 \cdot 10^{-2}$	1,122.66
0.25	0.26	0.17	0.2	$3.14 \cdot 10^{-2}$	$3.36 \cdot 10^{-2}$	1,141.31
$2.37 \cdot 10^{-2}$	$3.28 \cdot 10^{-2}$	$1.2 \cdot 10^{-2}$	$5.31 \cdot 10^{-2}$	$4.47 \cdot 10^{-2}$	$6.62 \cdot 10^{-2}$	1,163.3
$4.26 \cdot 10^{-2}$	$3.8 \cdot 10^{-2}$	0.18	0.17	$2.77 \cdot 10^{-2}$	$2.59 \cdot 10^{-2}$	1,199.44
$8.82 \cdot 10^{-2}$	$4.34 \cdot 10^{-2}$	$5.58 \cdot 10^{-2}$	$9.38 \cdot 10^{-2}$	$5.77 \cdot 10^{-2}$	$4.93 \cdot 10^{-2}$	1,202.53
0.2	0.21	0.12	0.15	$1.47 \cdot 10^{-2}$	$6.56 \cdot 10^{-2}$	1,537.01

Table A.4: Table 4 of galaxy clusters where shocks have been detected.

Appendix B

Derivations

B.1 Photon's Energy After Inverse Compton Scattering

$$\underbrace{\underline{p} = \left(\frac{E_e}{c}, \vec{p} \right)^T ; \underline{p}' = \left(\frac{E'_e}{c}, \vec{p}' \right)^T}_{\text{Electron}} \quad \& \quad \underbrace{\underline{q} = \left(\frac{E_\gamma}{c}, \frac{E_\gamma}{c} \vec{n} \right)^T ; \underline{q}' = \left(\frac{E'_\gamma}{c}, \frac{E'_\gamma}{c} \vec{n}' \right)^T}_{\text{Photon}} \quad (\text{B.1})$$

Where E_γ is the photon's energy, E_e the electron's energy, $|\vec{p}|$ is the electron's absolute momentum and γ is the Lorentz factor, with:

$$E_\gamma = h\nu; \quad E_e = \gamma m_e c^2; \quad |\vec{p}| = \gamma m_e c |\vec{\beta}|; \quad \gamma = \left(1 - \vec{\beta}^2 \right)^{-\frac{1}{2}}; \quad |\vec{\beta}| = \frac{|\vec{v}|}{c} \quad (\text{B.2})$$

\vec{n} is the unit vector pointing in the propagating direction. From the energy-momentum relation, the following expressions can be obtained:

$$p^2 = p'^2 = (m_e c)^2 \quad \& \quad q^2 = q'^2 = 0 \quad (\text{B.3})$$

From conservation of momentum, the following equality holds:

$$\underline{p}' = \underline{p} + \underline{q} - \underline{q}' \quad (\text{B.4})$$

$$(\underline{p}')^2 = (\underline{p} + \underline{q} - \underline{q}')^2 \quad (\text{B.5})$$

$$(\underline{p}')^2 = (\underline{p})^2 + (\underline{q})^2 + (\underline{q}')^2 + 2\bar{p}q - 2\bar{p}q' - 2\bar{q}q' \quad (\text{B.6})$$

$$0 = \bar{p}q - \bar{p}q' - \bar{q}q' \quad (\text{B.7})$$

Now, the mixed terms need to be calculated. It is crucial to use Minkowski spacetime $\eta = \text{diag}(+, -, -, -)$ for the following derivation.

$$\bar{p}q = \left(\frac{E_e}{c}, -\vec{p} \right) \left(\frac{E_\gamma}{c}, \frac{E_\gamma}{c} \vec{n} \right)^T \quad (\text{B.8})$$

$$= \frac{E_e E_\gamma}{c^2} - \frac{|\vec{p}| |\vec{n}| E_\gamma}{c} \cos \psi \quad (\text{B.9})$$

$$= \gamma m_e E_\gamma - \gamma m_e E_\gamma \beta \cos \psi \quad (\text{B.10})$$

$$= \gamma m_e E_\gamma (1 - \cos \psi) \quad (\text{B.11})$$

$$\underline{\bar{p}q'} = \left(\frac{E_e}{c}, -\vec{p} \right) \left(\frac{E'_\gamma}{c}, \frac{E'_\gamma \vec{n}'}{c} \right)^T \quad (\text{B.12})$$

$$\stackrel{(\text{B.11})}{=} \gamma m_e E'_\gamma (1 - \beta \cos \psi') \quad (\text{B.13})$$

$$\underline{\bar{q}q'} = \left(\frac{E_\gamma}{c}, \frac{E_\gamma \vec{n}}{c} \right) \left(\frac{E'_\gamma}{c}, \frac{E'_\gamma \vec{n}'}{c} \right)^T \quad (\text{B.14})$$

$$= \frac{E_\gamma E'_\gamma}{c^2} - \frac{E_\gamma E'_\gamma}{c^2} |\vec{n}| |\vec{n}'| \cos \varphi \quad (\text{B.15})$$

$$= \frac{E_\gamma E'_\gamma}{c^2} (1 - \cos \varphi) \quad (\text{B.16})$$

Re-expressing $\underline{\bar{p}q}$, $\underline{\bar{p}q'}$ and $\underline{\bar{q}q'}$ from Equation B.7 finally leads to

$$E'_\gamma = \frac{E_\gamma (1 - \beta \cos \psi)}{(1 - \beta \cos \psi') + \frac{E_\gamma}{E_e} (1 - \cos \varphi)} \quad (\text{B.17})$$

B.2 Rankine-Hugoniot Jump Conditions

For the jump conditions, following laws of conservation are required:

(i) Conservation of mass:

$$j = \rho_1 v_1 = \rho_2 v_2 \quad (\text{B.18})$$

(ii) Conservation of momentum:

$$p_1 + \rho_1 v_1^2 = p_2 + \rho_2 v_2^2 \quad (\text{B.19})$$

(iii) Conservation of energy flux:

$$\rho_1 v_1 \left(\frac{1}{2} v_1^2 + w_1 \right) = \rho_2 v_2 \left(\frac{1}{2} v_2^2 + w_2 \right) \quad (\text{B.20})$$

Further useful relations are:

a) Volume

$$V = \rho^{-1} \quad (\text{B.21})$$

b) Enthalpy per unit mass for perfect gas:

$$w_i = \frac{\gamma p_i V_i}{\gamma - 1} \quad (\text{B.22})$$

c) Perfect gas law:

$$\frac{p_1 V_1}{T_1} = \frac{p_2 V_2}{T_2} \quad (\text{B.23})$$

d) Mach number:

$$M = \frac{v}{c} = v \sqrt{\frac{\rho}{\gamma p}} \quad (\text{B.24})$$

$$j^2 \stackrel{(\text{B.18})}{=} \rho_1^2 v_1^2 \quad (\text{B.25})$$

$$\stackrel{(\text{B.19})}{=} \rho_1^2 (\rho_1^{-1} (p_2 - p_1 + \rho_2 v_2^2)) \quad (\text{B.26})$$

$$\stackrel{(\text{B.21})}{=} V_1^{-1} (p_2 - p_1 + V_2^{-1} V_1^2 j^2) \quad (\text{B.27})$$

$$\frac{p_2 - p_1}{V_1} = j^2 - \frac{j^2 V_2}{V_1} \quad (\text{B.28})$$

$$j^2 = \frac{p_2 - p_1}{V_1 - V_2} \quad (\text{B.29})$$

$$0 \stackrel{(B.20)}{=} w_1 - w_2 + \frac{1}{2}(v_1^2 - v_2^2) \quad (B.30)$$

$$\stackrel{(B.18),(B.21)}{=} w_1 - w_2 + \frac{1}{2}j^2(V_1^2 - V_2^2) \quad (B.31)$$

$$\stackrel{(B.22)}{=} \frac{\gamma}{\gamma-1}(p_1V_1 - p_2V_2) + \frac{1}{2}j^2(V_1 - V_2)(V_1 + V_2) \quad (B.32)$$

$$\stackrel{(B.29)}{=} 2\gamma(p_1V_1 - p_2V_2) + (\gamma-1)(p_2 - p_1)(V_1 + V_2) \quad (B.33)$$

$$= V_1(p_1(\gamma+1) + p_2(\gamma-1)) + V_2(p_1(1-\gamma) - p_2(\gamma+1)) \quad (B.34)$$

$$\frac{V_2}{V_1} = \frac{p_1(\gamma+1) + p_2(\gamma-1)}{p_1(\gamma-1) + p_2(\gamma+1)} \quad (B.35)$$

$$j^2 \stackrel{(B.29),(B.35)}{=} \frac{p_2 - p_1}{V_1 - V_1 \frac{p_1(\gamma+1) + p_2(\gamma-1)}{p_1(\gamma-1) + p_2(\gamma+1)}} \quad (B.36)$$

$$= \frac{(p_2 - p_1)(p_1(\gamma-1) + p_2(\gamma+1))}{V_1(p_1(\gamma-1) + p_2(\gamma+1) - p_1(\gamma+1) - p_2(\gamma-1))} \quad (B.37)$$

$$= \frac{(p_2 - p_1)(p_1(\gamma-1) + p_2(\gamma+1))}{2V_1(p_2 - p_1)} \quad (B.38)$$

$$= \frac{p_1(\gamma-1) + p_2(\gamma+1)}{2V_1} \quad (B.39)$$

$$v_1^2 \stackrel{(B.18)}{=} j^2V_1^2 \quad (B.40)$$

$$\stackrel{(B.39)}{=} \frac{1}{2}V_1(p_1(\gamma-1) + p_2(\gamma+1)) \quad (B.41)$$

$$\stackrel{(B.24)}{=} \frac{v_1^2(p_1(\gamma-1) + p_2(\gamma+1))}{2\gamma p_1 M^2} \quad (B.42)$$

$$2 = \frac{\gamma-1}{\gamma M^2} + \frac{p_2(\gamma+1)}{p_1 \gamma M^2} \quad (B.43)$$

$$\frac{p_2}{p_1} = \frac{2\gamma M^2 - (\gamma-1)}{\gamma+1} \quad (B.44)$$

$$\frac{\rho_2}{\rho_1} \stackrel{(B.21)}{=} \frac{V_1}{V_2} \quad (B.45)$$

$$\stackrel{(B.35)}{=} \frac{p_1(\gamma-1) + p_2(\gamma+1)}{p_1(\gamma+1) + p_2(\gamma-1)} \quad (B.46)$$

$$\stackrel{(B.44)}{=} \frac{(1+\gamma)M^2}{(\gamma-1)M^2 + 2} \quad (B.47)$$

$$= \frac{\gamma+1}{(\gamma-1) + 2/M^2} \quad (B.48)$$

$$\frac{T_2}{T_1} \stackrel{(B.23)}{=} \frac{p_2V_2}{p_1V_1} \quad (B.49)$$

$$\stackrel{(B.44),(B.48)}{=} \frac{(2\gamma M^2 - (\gamma-1))(2 + (\gamma-1)M^2)}{(\gamma+1)^2 M^2} \quad (B.50)$$

Now, considering strong shocks ($M \gg 1$) and monoatomic gas ($\gamma = 5/3$), following conditions are obtained:

$$\frac{p_2}{p_1} \stackrel{B.44}{=} \frac{2\gamma M^2}{\gamma + 1} = \frac{5}{4} M^2 \quad (\text{B.51})$$

$$\frac{\rho_2}{\rho_1} \stackrel{B.48}{=} \frac{v_1}{v_2} = \frac{\gamma + 1}{\gamma - 1} = 4 \quad (\text{B.52})$$

$$\frac{T_2}{T_1} \stackrel{B.50}{=} \frac{2\gamma(\gamma - 1)M^2}{(\gamma + 1)^2} = \frac{5}{16} M^2 \quad (\text{B.53})$$

Acknowledgements

Der größte Meilenstein des gesamten Bachelorstudiums ist vermutlich, sowohl für jeden Studenten, als auch für mich, das Verfassen einer Bachelorarbeit. Ich habe mich sowohl mit Freude, als auch mit Nervosität nach diesem Moment gesehnt, die letzten Schritte meines Studiums beschreiten zu dürfen. Glücklicherweise haben mir meine beiden Betreuer, Dr. Klaus Dolag und Ludwig Böss, diese Nervosität schnell genommen und mir die faszinierende Welt der *Computational Astrophysics* gezeigt.

Zuerst möchte ich Dr. Klaus Dolag danken. Das Vertrauen, welches in mich gesteckt wurde, diese Bachelorarbeit zu verfassen, hat mich immer wieder motiviert, so viel Zeit und Fleiß wie nur möglich in diese Arbeit zu stecken. Ich möchte mich für die vielen hilfreichen Anregungen und unterstützende Worte bei noch so kleinen Fortschritten meiner Arbeit bedanken. Für das Integrieren in der CAST Gruppe bin ich sehr dankbar und auch gerührt darüber, mich in ein so persönliches Arbeitsklima zu involvieren. Es hat mir jedes mal viel Freude bereitet, an den Treffen der Gruppe teilzunehmen.

Vielen Dank an Ludwig Böss, nicht nur für die Betreuung dieser Arbeit, sondern auch als Wegweiser. Dank eines Tutoriums, welches er vor einem Jahr gehalten hat, bin ich auf diese Form der Astrophysik mit großer Faszination aufmerksam geworden. Zudem möchte ich mich sehr für seine Bereitschaft bedanken, mir so intensiv bei meinen Coding-Problemen, mit dem Korrekturlesen und vielen anderen Hindernissen geholfen zu haben.

Dass ich so regelmäßig wertvollen Input für das weitere Vorgehen meiner Bachelorarbeit erhalten habe und so viel Zeit und Aufwand in mich und meine Arbeit durch die wöchentlichen Treffen gesteckt wurde, rechne ich Klaus und Ludwig hoch an. Die Bereitschaft mir bei Problemen zu helfen, war immer hoch und das weiß ich sehr zu schätzen.

Auch bei Tadzju Hoffmann möchte ich mich für das Erstellen meines persönlichen USM Accounts bedanken.

Bei der gesamten CAST Gruppe möchte ich mich bedanken, mich so herzlich aufgenommen und mir schnell mit freundlichen Worten meine Unsicherheit als "Frischling" genommen zu haben. Die Liebe zum Fach, welche ich von jedem einzelnen der Gruppe vermittelt bekommen habe, hat mich auch in meiner Arbeit immer wieder angetrieben. Die tollen und interessanten Gespräche werden mir immer in Erinnerung bleiben.

Zusätzlich möchte ich mich bei Paul Jakobs für das Lektorat meiner Arbeit bedanken.

Zu guter Letzt möchte ich mich bei meinen Freunden und meiner Familie bedanken, denen ich mit Gesprächen über meine Bachelorarbeit regelmäßig auf den Zeiger gehen durfte. Auch

die anerkennende Unterstützung hat mir sehr viel Stärke und Durchhaltevermögen gegeben.

Dank der Unterstützung all dieser Menschen wäre die Arbeit so nicht möglich gewesen. Euch allen habe ich zu verdanken, dass ich meinem Traum so viel wie nur möglich über die Astrophysik zu erfahren immer näher komme.

Selbständigkeitserklärung

Ich versichere hiermit, die vorliegende Arbeit mit dem Titel

**Shocks and Corresponding Physical Properties of Merging Galaxy Clusters in
*Magneticum***

selbständig verfasst zu haben und keine anderen als die angegebenen Quellen und Hilfsmittel verwendet zu haben.

Vorname Name

München, den 16. Juli 2021